Towards a Remote Sensing Solution to Quantify Nitrous Oxide Emissions by Integrating Shortwave and Thermal Infrared Bands

Ayesha Riaz[1], Kang Sun[1,2], Brian D. Baker[3], Brian Buma[4], Karen E. Cady-Pereira[5], Christopher Chan Miller[3,6,7,8], William C. Eddy III[9], Betsy M. Farris[3], Thomas U. Kampe[3], Eric A. Kort[10, 11], Nathan P. Leisso[3], Robert Spurr[12], Emily R. Stuchiner[13], and Wendy H. Yang[9]

[1]Department of Civil, Structural and Environmental Engineering, University at Buffalo, Buffalo, NY, USA
[2]Research and Education in Energy, Environment and Water Institute, University at Buffalo, Buffalo, NY, USA
[3]BAE Systems, Boulder, CO, USA
[4]Environmental Defense Fund, New York, NY, USA
[5]Atmospheric and Environmental Research, Lexington, MA, USA
[6]Harvard John A. Paulson School of Engineering and Applied Sciences, Harvard University, Cambridge, MA, USA
[7]Center for Astrophysics | Harvard & Smithsonian, Cambridge, MA
[8]Climate Change Research Centre, University of New South Wales, Kensington, NSW, Australia
[9]Department of Plant Biology, University of Illinois Urbana-Champaign, Urbana, IL, USA
[10]Department of Climate and Space Sciences and Engineering, University of Michigan, Ann Arbor, MI, USA
[11]Atmospheric Chemistry Department, Max Planck Institute for Chemistry, Mainz, 55128, Germany
[12]RT Solutions, Cambridge, MA, USA
[13]Renewable and Sustainable Energy Institute, University of Colorado, Boulder, CO, USA

Correspondence: Kang Sun (kangsun@buffalo.edu)

Abstract. Nitrous oxide (N_2O) is a potent greenhouse gas whose emissions are dominated by natural and agricultural soils and are highly heterogeneous and episodic, yet existing observational techniques lack the spatial coverage and near-surface sensitivity needed to resolve this variability. In this study, we evaluate a remote sensing framework that integrates shortwave infrared (SWIR) and thermal infrared (TIR) spectral bands to enhance the detectability of column-integrated N_2O mixing ratio (X_{N_2O}). To implement this, we expand the capacity of ~~the~~ Smithsonian PLanetary ATmosphere–Vector Linearized Discrete Ordinate Radiative Transfer (SPLAT–VLIDORT~~radiative transfer~~) model to jointly simulate both spectral regions and apply linear sensitivity analysis to quantify the X_{N_2O} measurement error and vertical sensitivity under realistic environmental conditions and instrumental designs. This framework is applied to both airborne and spaceborne instruments to evaluate the influence of platform characteristics on retrieval performance. The joint SWIR–TIR setting improves near-surface sensitivity relative to the TIR band alone while maintaining the low X_{N_2O} measurement error. It achieves single-sounding measurement error of approximately 3.2 ppb for an airborne instrument with a ground footprint size of 20 m and 1.1 ppb for spaceborne instrument with a footprint size of 0.7 km, while retaining sensitivity to the near-surface layers. Assuming X_{N_2O} variability is observable at twice the precision, natural X_{N_2O} variability inferred from in situ aircraft N_2O observations in the US Midwest becomes observable beyond spatial aggregation scales of $\sim$ 2.5 km for airborne and $\sim$ 22 km for spaceborne instruments, subject to significant X_{N_2O} variation between flights. An independent, emission-based detectability analysis indicates that X_{N_2O} variability induced by uniform emissions of 5 nmol m^{-2} s^{-1} becomes observable beyond spatial averaging of about 2.1 km for airborne and 8.4 km for spaceborne instruments. Together, these results constitute a quantitative basis for N_2O detectability

using a joint SWIR–TIR setting, with a focus on diffuse soil emissions that are more difficult to detect yet dominate the global N_2O budget, and they provide practical guidance for future N_2O dedicated missions.

1 Introduction

Nitrous oxide (N_2O) is the third most important anthropogenic greenhouse gas after carbon dioxide (CO_2) and methane (CH_4) (Weber et al., 2024; Feng and Li, 2023), currently accounting for approximately 7% of the net anthropogenic radiative forcing (3.22 W m^{-2}) of the Earth's climate system (Feng and Li, 2023; IPCC, 2021). It has a global warming potential of roughly 273 times greater than CO_2 over a 100-year timescale (Weber et al., 2024) and an atmospheric lifetime of 116 ± 9 years (Prather et al., 2015), primarily due to its slow removal via photolysis in the stratosphere (Tian et al., 2020). Anthropogenic activities including fuel combustion, agriculture, and industrial processes have substantially increased the N_2O emissions (Smith, 2017; Jovani-Sancho et al., 2023), with nitrogen-based fertilizers used in agriculture being the major contributor (Thompson et al., 2019; Tian et al., 2020). In the global N_2O budget at about 19 TgN yr^{-1}, natural soil emissions dominate the N_2O sources at about 6–7 TgN yr^{-1}, followed by agricultural emissions ranging from 4.3 to 5.8 TgN yr^{-1} (Syakila and Kroeze, 2011). Atmospheric N_2O concentrations have already exceeded those projected under the most pessimistic scenario of the Shared Socioeconomic Pathway (SSP5-8.5), suggesting that current emission trajectories surpass both policy expectations and model projections (Tian et al., 2024). This is further reinforced by Microwave Limb Sounder (MLS) observations from 2005–2021, which reveal a growing stratospheric sink for N_2O, implying that actual emissions may be higher than those inferred from concentration data alone (Prather et al., 2023).

A variety of observational techniques have been used to quantify N_2O emissions and characterize their spatiotemporal variability. Chambers are widely employed for agricultural field-scale studies (Zhang et al., 2024; Kong et al., 2025; Zimbron et al., 2025), offering high precision at fine temporal resolution, but they are effectively point measurements and are not representative of broader heterogeneous landscapes. Ground-based Eddy Covariance (EC) systems provide continuous flux measurements over larger footprints (~ 1 km^2 scale), capturing ecosystem-scale dynamics, but their fixed-point nature limits spatial coverage (Murphy et al., 2022; Pan et al., 2022; Rana et al., 2025; Tikkasalo et al., 2025). Airborne EC campaigns overcome this limitation by measuring fluxes over tens to hundreds of kilometers and have been particularly effective in agricultural regions, although their deployment remains logistically complex and resource-intensive (Wilkerson et al., 2019; Waldmann et al., 2026). Similarly, airborne or tall tower-based in situ measurements combined with atmospheric transport and inversion models provide valuable top-down estimates of regional emissions, offering a complement to inventory-based approaches (Kort et al., 2017; Dacic et al., 2024; Gvakharia et al., 2020; Xiang et al., 2013; Griffis et al., 2019; Haszpra et al., 2018; Kort et al., 2011; Chen et al., 2016b). Despite these advances, accurately capturing soil N_2O emissions, complicated by their episodic and spatially heterogeneous nature (Molodovskaya et al., 2012; Ackett et al., 2025; Zhang et al., 2024; Zhou et al., 2022; Shrestha and Wang, 2018), remains a major challenge, underscoring the need for scalable observational strategies with improved spatial resolution.

Remote sensing of greenhouse gases on spaceborne or airborne platforms offers a powerful alternative to overcome these spatiotemporal limitations, by providing coverage up to the global scale and allowing the detection of long-term trends and multiscale emission patterns (Jacob et al., 2016). Remote sensing instruments typically observe the dry air column-integrated mixing ratio of greenhouse gases, conventionally denoted as "X" followed by the molecule name, e.g., X_{N_2O} for N_2O. These column amounts are insensitive to the vertical distributions of trace species and thus more closely related to emissions than point-based volume mixing ratios (Chen et al., 2016a). Over the recent decade, missions such as the Orbiting Carbon Observatories (OCO-2 & OCO-3) (Crisp, 2015; Crisp et al., 2017; Eldering et al., 2019; Taylor et al., 2023), TROPOspheric Monitoring Instrument (TROPOMI) (Lorente et al., 2021), Greenhouse Gases Observing Satellite (GOSAT) series (Butz et al., 2011; Suto et al., 2021), and MethaneSAT (South, 2024) deliver high-precision ~~CO_2 and CH_4~~ X_{CO_2} and X_{CH_4} retrievals and have demonstrated the ability to detect and quantify emissions from global to sub-kilometer scales. Airborne platforms provide complementary capabilities by targeting high-resolution observations at finer spatial scales. For example, MethaneAIR, an airborne precursor to MethaneSAT, provides a fine spatial resolution of 20×20 m^2 with overall X_{CH_4} retrieval accuracy within $\sim$1% when validated against ground-based spectrometers (Chan Miller et al., 2024; Chulakadabba et al., 2023).

In contrast, there exists no dedicated remote sensing mission for N_2O (Ricaud et al., 2021). In the shortwave infrared (SWIR) spectral region, where CO_2 and CH_4 instruments have achieved remarkable success, the most detectable N_2O band near 2.3 μm is weak and subject to significant interference from CH_4 bands. Stronger N_2O features are found in the thermal infrared (TIR) near 4.4 or 7.8 μm, but TIR observations have limited sensitivity to near-surface layers, which matter the most for emission detection. In addition, the relative emission-induced enhancements to the N_2O column are generally lower than those of CH_4 and CO_2, and in this regard, N_2O has been proposed as a light-path proxy for CH_4 and CO_2 retrievals (Frankenberg et al., 2025). For example, the peak-to-peak variability of N_2O volume mixing ratio observed in the planetary boundary layer (PBL) over a source region is only a few ppb (Dacic et al., 2024), which translates to an X_{N_2O} variability of about 1 ppb, or 0.3% of the X_{N_2O} background. This makes N_2O sources more difficult to detect than CO_2 or CH_4 even given comparable instrument sensitivity. As secondary products, N_2O abundance has been retrieved from existing satellite-observed spectra in both SWIR and TIR bands. The SCanning Imaging Absorption SpectroMeter for Atmospheric CHartographY (SCIAMACHY) offered one of the first N_2O detection capabilities in SWIR region. With a target precision of approximately 10% in the retrieved N_2O column amount, the SCIAMACHY N_2O product is insufficient for detecting localized enhancements (Dils et al., 2006). Infrared sounders primarily designed for numerical weather prediction, such as the Atmospheric Infrared Sounder (AIRS) and the Infrared Atmospheric Sounding Interferometer (IASI), have improved upon SCIAMACHY with typical N_2O precision close to 1% (Xiong et al., 2014; Vandenbussche et al., 2022). However, their coarse spatial resolution and limited near-surface sensitivity make them poorly suited for detecting localized N_2O emission sources. For the first time, the GOSAT-2 satellite covers both SWIR and TIR N_2O bands with the same instrument, but its coarse footprint diameter of ~ 10 km and sparse sampling geometry limit its ability to resolve localized and spatially heterogeneous N_2O enhancements (Suto et al., 2021). Using only the SWIR N_2O band of GOSAT-2, Noël et al. (2022) provided the first X_{N_2O} product from GOSAT-2 with single-sounding precisions of about 4–9 ppb. Still, current spaceborne N_2O instrumentation cannot be used to study agricultural emissions, which triggers attempts to use other high-resolution nitrogen species as a proxy (Adams et al., 2026).

Leveraging the heritages of existing greenhouse gas instruments, especially MethaneAIR and MethaneSAT, this study presents a dual SWIR–TIR band concept applicable for both airborne and spaceborne N_2O remote sensing instruments. Similar to MethaneAIR and MethaneSAT, this concept employs high spatial resolution (footprint sizes of about 20 m for airborne and 0.7 km for spaceborne instruments), wide swath imaging grating spectrometer designs for the ability to detect both emission hot spots (Warren et al., 2025) and dispersed sources (MacKay et al., 2026). The coverage of the SWIR N_2O band at 2.3 μm offers near-uniform vertical sensitivity desirable for emission quantification. The ~~stronger~~ TIR N_2O band at 7.8 μm ~~provides~~ is selected to provide crucial observational constraints to X_{N_2O}, additional to the weak SWIR band. Although N_2O also exhibits strong absorption features near 4.4 μm, the 7.8 μm region was selected to avoids mixed solar-thermal radiance contributions and potential non-Local Thermodynamic Equilibrium (non-LTE) effects (Barnet et al., 2023). For the first time, we enhance the Smithsonian PLanetary ATmosphere–Vector Linearized Discrete Ordinate Radiative Transfer (SPLAT–VLIDORT), the radiative transfer model underpinning the MethaneAIR and MethaneSAT retrieval algorithms (Chan Miller et al., 2024), to enable a joint SWIR–TIR retrieval. Linear sensitivity analysis based on this enhanced radiative transfer framework demonstrates that the integration of SWIR and TIR bands yields significantly improved N_2O precision and PBL sensitivity relative to the limiting single-band case, an advantage similarly seen in the multispectral CO retrieval in the Measurements of Pollution in the Troposphere (MOPITT) instrument (Worden et al., 2010).

To assess the N_2O detectability by the proposed instruments under realistic conditions, we approximate real-world X_{N_2O} variability in two complementary ways. The first is to assume X_{N_2O} covaries with PBL N_2O mixing ratio, which was extensively sampled by an aircraft during the Measurement of Agriculture Illuminating farm-Zone Emissions of N_2O (MAIZE) campaign over the US Midwest. The second is to transform a range of hypothetical N_2O emissions that are informed by autochamber flux data to X_{N_2O} enhancements at various spatial scales. These X_{N_2O} variabilities are then compared with X_{N_2O} measurement error at common spatial scales to infer detectability. Together, these results establish the scientific basis for N_2O remote sensing missions dedicated to detect and quantify agricultural soil N_2O emissions at spatial scales relevant to emissions monitoring and management, providing practical guidance for instrument design aimed at closing existing gaps in N_2O monitoring. By treating agricultural N_2O emissions as the primary design case, the proposed instrument capable of resolving the most challenging sources will also be well suited for other stronger emission sectors such as industrial.

2 Data

This section presents the three observational datasets used in this study. First, satellite-retrieved atmospheric state data from the Cross-track Infrared Sounder (CrIS) provide ~~profiles of temperature and~~ surface temperature, profiles of key absorbers (N_2O, CH_4, and H_2O) ~~in the SWIR and TIR bands, which~~ and temperature, along with the surface emissivity used for the TIR band simulations. For SWIR, a representative grass albedo from the Terra Advanced Spaceborne Thermal Emission and Reflection Radiometer (ASTER) climatology is assumed, with values ranging from 0.146 to 0.171 over the selected SWIR spectral window. These quantities define the atmospheric and surface conditions for forward radiative transfer modeling (Section 3.1.4) ~~and~~ in the SWIR and TIR spectral regions and allow estimation of prior error structures (Section 3.1.2). In combination with

the instrument noise characteristics (Section 3.1.3), these lead to the X_{N_2O} measurement error estimation for the proposed instruments. Second, airborne in-situ measurements from the MAIZE campaign (Section 2.2) capture high-resolution N_2O variability within the PBL over a major agricultural region, shedding light on the X_{N_2O} spatial heterogeneity using semivariograms (Section 3.2). Although the CrIS and MAIZE datasets are not colocated in time and space, both are representative of summertime agricultural conditions over the US Midwest dominated primarily by corn and soybean croplands. These datasets are used as complementary constraints for realistic environmental variability rather than for direct scene-by-scene comparison. Third, hourly N_2O flux measurements by autochambers distributed in a commercial farm in Illinois (Section 2.3) provide realistic spatiotemporal variability of soil N_2O emissions, putting the detectability of N_2O emissions into a real-world context (Section 3.3).

2.1 Realistic geophysical quantities from CrIS Level 2 product

Level 2 data from the CrIS instrument onboard NOAA's JPSS satellites are used to construct realistic profiles of trace gases (N_2O, CH_4, H_2O) and temperature as well as surface temperature and emissivity useful for the TIR radiative transfer modeling. This study leverages 100 CrIS soundings over the US Midwest acquired on 23 August 2023. The selected date provides a large number of clear-sky soundings spanning a wide range of thermal contrast (2–12 K), providing a representative sample of US Midwest summertime conditions for evaluating retrieval sensitivity. Figure 1 shows the spatial distribution of the selected CrIS pixels, color-coded by thermal contrast, which is defined as the difference between retrieved surface temperature and that of the lowest atmospheric layer. ~~These soundings span a wide range of thermal contrast (2–12 K), providing a representative sample of summer conditions for evaluating retrieval sensitivity.~~ The selected region in Fig.1 is dominated by agricultural land cover, primarily corn and soybean croplands. Thermal contrast is most important for the TIR band, as it governs the strength of the upwelling signal and thus influences vertical sensitivity. The prior error matrices for H_2O and temperature profiles available in the CrIS Level 2 data are used to set a priori constraints in the linear sensitivity study (see Section 3.1.2).

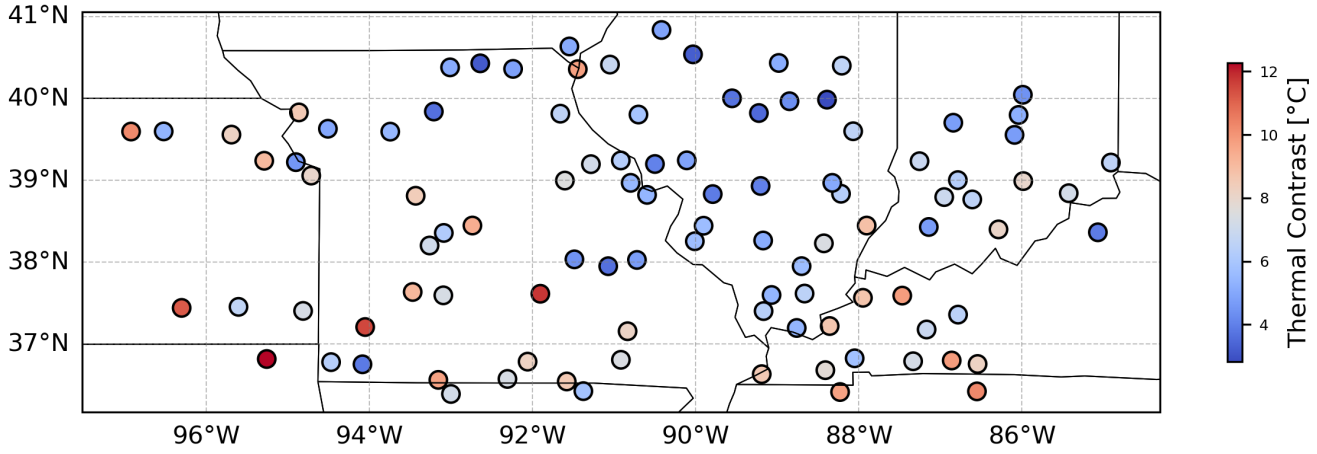

Figure 1. Spatial distribution of 100 CrIS soundings over the US Midwest on 23 August 2023, color-coded by thermal contrast. These pixels span a wide range of thermal contrast from 2–12 K.

2.2 MAIZE aircraft campaign in situ measurements

Airborne in-situ measurements of N_2O were conducted over the state of Iowa, located within the corn belt of United States ($41°$ to $43.5°$N and $92°$ to $95°$W), in 2022 as part of the MAIZE campaign. A total of eight research flights took place between 18 and 30 May 2022 using a Mooney aircraft operated by Scientific Aviation, Inc. Flights were conducted during growing season under fair weather conditions, avoiding active precipitation, low visibility events, and on days with steady winds. This period, characterized by recent fertilizer application and warm and moist conditions was conducive to elevated N_2O emissions from cropland soils. Each flight lasted around 5–6 hours and was conducted between 11:00 and 18:00 local time to ensure sampling within a well-developed PBL. The aircraft flew at an average altitude of $\sim$ 475 m above ground level (AGL), with transects oriented perpendicular to the prevailing wind direction to enhance sensitivity to surface fluxes. Two vertical profiles were captured during each flight to characterize the PBL structure. The primary target species, N_2O, was measured using a Los Gatos Research (LGR) N_2O/CO Analyzer (model 916-0015), which also recorded H_2O and CO. In addition, CH_4 and CO_2 were measured using a Picarro G2401–m analyzer (Dacic et al., 2024). The N_2O in situ measurements are used to approximate column-integrated mixing ratio of N_2O and analyze its spatial variability. Figure 2a shows the area coverage for each flight and Fig. 2b indicates the corresponding in situ N_2O mixing ratios measured during each flight. ~~The~~ Figure 2b has two vertical axes, with the left and right axes showing in situ N_2O mixing ratio in ppb for alternating flights to improve readability. In both panels, faint lines indicate vertical profile segments and bold lines mark the horizontal PBL transects used to quantify X_{N_2O} variability for the semivariogram-based detectability analysis.

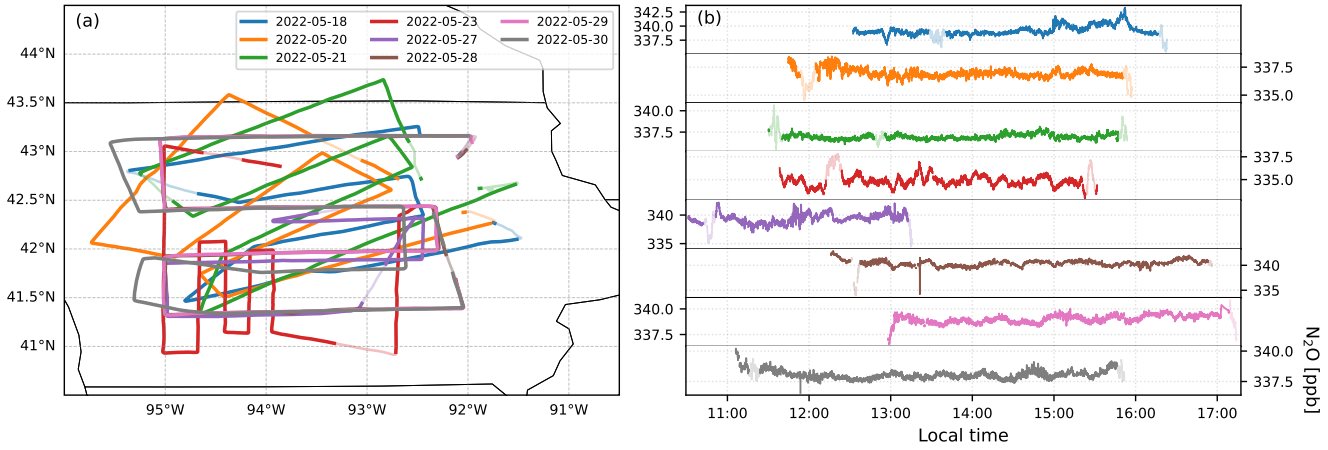

Figure 2. (a) Flight tracks during the MAIZE campaign over the state of Iowa in May 2022. (b) Corresponding time series of in situ N_2O mixing ratios. ~~Faint~~ Both vertical axes represent the in situ N_2O mixing ratio in ppb. The left and right axes are used for alternating flight days to reduce overlap and improve readability. In both panels, faint lines represent vertical profile segments, while bold lines highlight horizontal flight path within the PBL used to calculate X_{N_2O} variability for detectability analysis. Colors distinguish individual flight days and are consistent between panels.

2.3 Autochamber flux data

Hourly N_2O fluxes were measured from May 2022 to April 2023 in a conventionally-tilled maize field near Villa Grove, Illinois, using 16 automated chambers. To capture spatial and temporal variability of emissions, the chambers were distributed across four sampling nodes within ∼5 ha area, with nodes spaced 50–100 m apart (Fig. 3a inset). Each node contained four chambers radially positioned 12 m from a central N_2O gas analyzer (LI-7820, LI-COR Biosciences), which sequentially sampled the fluxes using an automated multiplexer (LI-8250). Chamber collars (20 cm diameter) were permanently installed adjacent to crop rows, ensuring that no vegetation was present within the chamber footprint and that chambers remained fully open between measurements in order to avoid shading or disturbance. Figure 3a shows the spatiotemporal variation of measured N_2O flux across four nodes, where chambers in the same node are averaged and then aggregated to 6-hour intervals to enhance visualization. Data are missing for approximately three weeks in October–November 2022 due to instrument maintenance and crop harvest (Stuchiner et al., 2025). Figure 3b zooms in over a high emission event of 21–25 May 2022 to highlight the hourly variability of N_2O emissions. The node-wise average time series are shown as solid lines, while the maximum and minimum chamber values within each node are shown as dashed lines. The thick grey line represents the overall hourly flux averaged over all nodes which remain mostly above 5 nmol m^{-2} s^{-1} and occasionally exceed 10 nmol m^{-2} s^{-1} in this period.

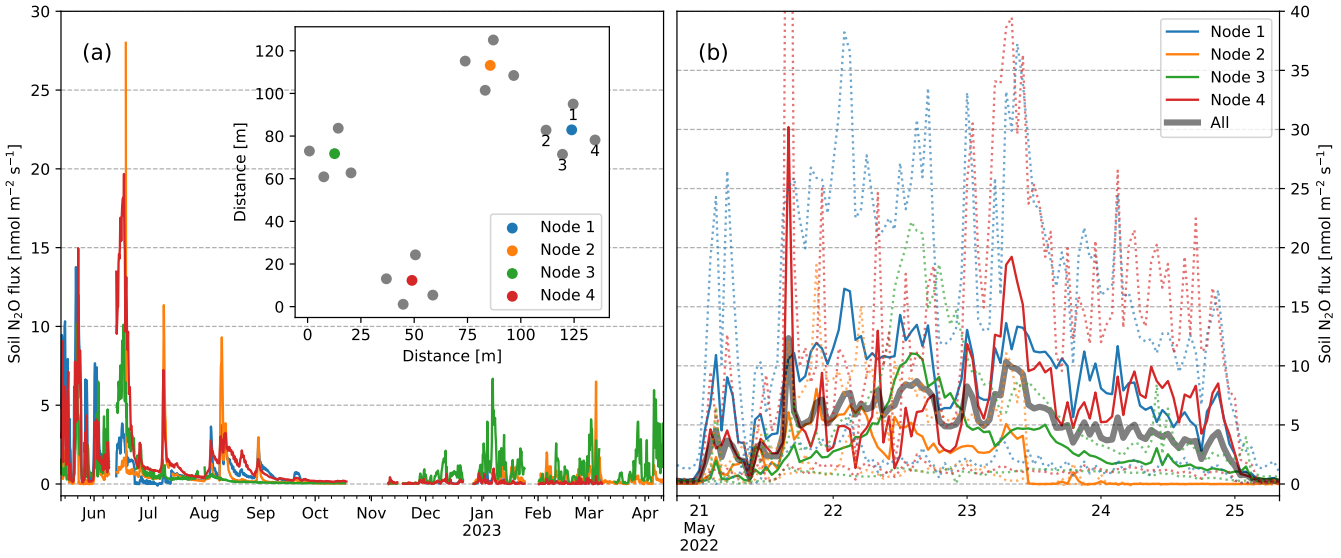

Figure 3. Time series of soil N_2O flux (nmol m^{-2} s^{-1}) measured from May 2022 to April 2023 using automated chambers deployed at four nodes in a conventionally tilled maize field near Villa Grove, Illinois. (a) Node-averaged fluxes at 6-hourly resolution showing the temporal and spatial variability, with distinct emission pulses during the early growing season. The inset shows the spatial arrangement of nodes and chambers within an area of ∼5 ha. (b) Expanded view of 21–25 May 2022, highlighting the hourly flux variability. Solid lines represent node-averaged fluxes, dashed lines denote the minimum and maximum chamber values within each node, and the thick grey line represents the average across all nodes.

3 Measurement Methodology

This section combines theoretical analysis and empirical data to evaluate the capability of potential dual-band remote sensing instruments for detecting N_2O emissions on both airborne and spaceborne platforms. Section 3.1 introduces the linear sensitivity analysis framework, which takes a Bayesian approach to quantify X_{N_2O} measurement error and vertical sensitivity based on instrument design parameters, a priori constraints, and radiative transfer simulations. Section 3.2 leverages in situ airborne N_2O measurements from the MAIZE campaign to approximate spatial variability of X_{N_2O} and characterize how this variability compares with measurement error at different spatial scales. Finally, Section 3.3 compares emission-driven column enhancement against measurement error. Both Sections 3.2 and 3.3 aim to provide a quantitative basis for the detectability of N_2O emissions by the proposed instruments.

3.1 Linear sensitivity analysis

3.1.1 Theory

As articulated in Rodgers (2000), the linear sensitivity analysis framework assumes that the perturbations to a vector of observations $\mathbf{y}$ are linear relative to the perturbations of a state vector $\mathbf{x}$. In other words, the Jacobian

$$\mathbf{K} = \frac{\partial \mathbf{y}}{\partial \mathbf{x}} \tag{1}$$

is approximately constant within the error range of $\mathbf{x}$. Here, $\mathbf{y}$ is the expected values of a spectrum observed by a remote sensing instrument with Gaussian error covariance matrix $\mathbf{S_o}$, and the state vector consists of the volume mixing ratio profiles of N_2O, CH_4, and H_2O, atmospheric temperature profile, and the surface temperature. We assume a priori knowledge of $\mathbf{x}$ as a Gaussian distribution with mean value $\mathbf{x_a}$ and a covariance matrix of $\mathbf{S_a}$. Within the Bayesian framework, $\mathbf{S_a}$ represents the prior uncertainty of the state vector. Practically, it also acts as a regularization whose strength can be controlled by multiplying $\mathbf{S_a}$ by a scaling factor, as implemented in Section 4.1. The a priori profiles are adopted from CrIS Level 2 products as mentioned in section 2.1. The prior error matrices are constructed in a similar manner to those deployed in the MethaneAIR/GOSAT algorithms for N_2O and CH_4 profiles and extracted from CrIS Level 2 product for H_2O and atmospheric temperature profiles (see section 3.1.2). The observation error $\mathbf{S_o}$ is constructed based on the instrument specification given in section 3.1.3. The Jacobian $\mathbf{K}$ is calculated using the radiative transfer model detailed in section 3.1.4.

Applying the Bayes' theorem, the state vector can be retrieved from the observation and the prior:

$$\hat{\mathbf{x}} = \mathbf{x_a} + \mathbf{G}(\mathbf{y} - \mathbf{K}\mathbf{x_a}), \tag{2}$$

where

$$\begin{aligned}\mathbf{G} &= \frac{\partial \hat{\mathbf{x}}}{\partial \mathbf{y}} \\ &= \mathbf{S_a}\mathbf{K}^{\mathrm{T}}\left(\mathbf{K}\mathbf{S_a}\mathbf{K}^{\mathrm{T}} + \mathbf{S_o}\right)^{-1}\end{aligned} \tag{3}$$

is the gain matrix. Here, T denotes matrix transpose. The measurement error is linearly propagated from the observation to the retrieved state vector:

$$\mathbf{S_m} = \mathbf{G}\mathbf{S_o}\mathbf{G}^{\mathrm{T}}. \tag{4}$$

Our goal is to retrieve X_{N_2O}, which can be written as a function of the retrieved state vector:

$$X_{N_2O} = \mathbf{h}^{\mathrm{T}}\hat{\mathbf{x}}. \tag{5}$$

Currently, we assume X_{N_2O} only depends on the retrieved N_2O mixing ratio profile, so the weighting vector $\mathbf{h}$ is the fractional dry air column at the corresponding ~~layer~~ layers of the N_2O profile and zero ~~otherwise~~for all other elements of the state vector,

such that only N_2O profile contributes to the calculation of X_{N_2O}. The measurement error of X_{N_2O} is then linearly propagated from the state vector measurement error:

$$\sigma_{X_{N_2O}} = \mathbf{h}^{\mathrm{T}}\mathbf{S_m}\mathbf{h}. \tag{6}$$

This measurement error, or precision of X_{N_2O}, is influenced by interference errors associated with the variabilities and sensitivities of the other retrieved state vector elements through the gain matrix (Connor et al., 2016). However, the interference errors from the non-N_2O state vector elements are at least one order of magnitude smaller than the N_2O measurement error, indicating that their contributions are minimal compared to the dominant N_2O measurement uncertainty. $\sigma_{X_{N_2O}}$ is a fundamental design parameter for any N_2O instrument as it limits the observable variability of X_{N_2O} by instrument noise. However, $\sigma_{X_{N_2O}}$ does not inform the different detectability at different part of the atmosphere. When the a priori is dominant, the retrieval precision mostly reflects the a priori uncertainty. As such, we will leverage the averaging kernel matrix, which represents the sensitivity of the retrieved state to the true atmosphere state and is given by

$$\begin{aligned}\mathbf{A} &= \frac{\partial \hat{\mathbf{x}}}{\partial \mathbf{x}} \\ &= \mathbf{GK}.\end{aligned} \tag{7}$$

X_{N_2O} as a derived quantity from the retrieved state can then be evaluated using the column averaging kernel vector $\mathbf{a}$. The element of the column averaging kernel for the lth N_2O layer is

$$\mathbf{a}_l = \frac{1}{\mathbf{h}_l}(\mathbf{h}^{\mathrm{T}}\mathbf{A})_l, \tag{8}$$

in which the subscript l only indexes the elements related to the N_2O profile. For a particular layer, a column averaging kernel value equaling 1 represents the ideal case, where the retrieved X_{N_2O} responds to changes in N_2O mixing ratio profile exactly as the true value of X_{N_2O}. A column averaging kernel value smaller than 1 indicates that the retrieved X_{N_2O} is less sensitive to N_2O in that layer, and that the a priori N_2O profile element is a significant contributor. We use the mean column averaging kernel values of the bottom two layers (roughly the bottom 1 km) as the indicator of the retrieved X_{N_2O}'s sensitivity to near-surface N_2O. A desirable instrument design should have a low X_{N_2O} measurement error and a near-surface column averaging kernel value close to 1.

3.1.2 A priori constraint

The prior error covariance matrix $\mathbf{S_a}$ is a crucial element in the regularization of the retrieval, as it balances the contributions from the observation and the prior. ~~To capture realistic variability~~Since no mature operational N_2O covariance structure is currently available, we adopt the MethaneAIR CH_4 a priori error covariance matrix (Chan Miller et al., 2024), which originates from the GOSAT CH_4 algorithm developed by the University of Leicester (Parker et al., 2020), for both N_2O and CH_4 profiles. Similar to Chan Miller et al. (2024), we decompose the error covariance matrix into a standard deviation profile and an error correlation matrix. The N_2O standard deviation profile, shown in Fig. 4a, is scaled down from the original CH_4 standard

deviation profile by a factor of 5.76 based on the ratio between typical atmospheric abundance of CH_4 (∼1900 ppb) and N_2O (∼330 ppb), reflecting the lower atmospheric abundance of N_2O. The ~~error~~ purpose of adopting this scaled CH_4 prior covariance structure here is not to reproduce the exact climatological variability of atmospheric N_2O, which is expected to be smaller than the prior standard deviation shown in Fig. 4a. Instead, the intention was to provide a reasonable regularization for evaluating retrieval sensitivity to the a priori constraint. Using the realistic N_2O variability as prior error would strongly constrain the retrieval toward the prior state, substantially reducing averaging kernel sensitivity and limiting the information from observations. Section 4.1 further evaluates this tradeoff by continuously scaling the prior strength.

The error correlation matrix is the same for N_2O and CH_4 and is shown in Fig. 4b. This choice is justified by the fact that both N_2O and CH_4 are long-lived, well-mixed gases with similar vertical distribution patterns in the troposphere and stratosphere.

For H_2O and temperature, the prior error covariance matrices are adopted from the CrIS Level 2 product (Section 2.1) and similarly decomposed into standard deviation profiles and error correlation matrices in Fig. 4c-f. The CrIS Level 2 algorithm operates in logarithmic space for trace gases, so the H_2O profile standard deviation is converted from relative error to absolute error, in mixing ratio unit, using the CrIS posterior H_2O profile. In addition to atmospheric profiles, the surface temperature is included in the state vector, along with a loose 10% prior error.

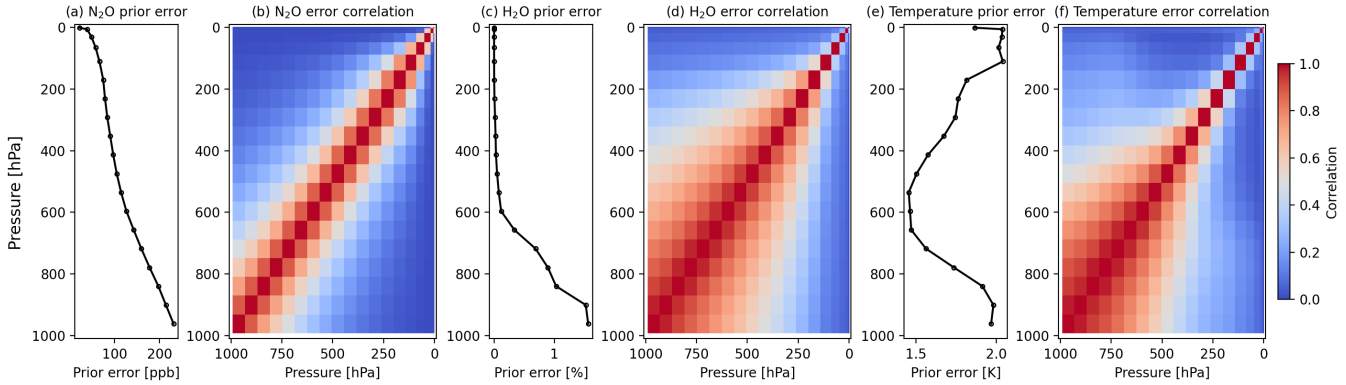

Figure 4. Prior error covariance matrices, decomposed to standard deviation profiles and error correlation matrices, for atmospheric profiles in the state vector. Panels a, c, and e show the error standard deviation profiles for N_2O, H_2O, and temperature, respectively. Panels b, d, and f present the corresponding error correlation matrices. The N_2O prior error is constructed by scaling down the CH_4 standard deviation from the MethanAIR and GOSAT algorithms while keeping the same correlation matrix. H_2O and temperature priors are adopted from the CrIS Level 2 product.

3.1.3 Instrument design parameters and observational constraints

For potential airborne and spaceborne N_2O-observing instruments, we assume push-broom, imaging grating spectrometer designs similar to those in MethaneAIR and MethaneSAT (Staebell et al., 2021; Chan Miller et al., 2024). The instrument specifications are chosen from currently available technologies and detailed in Table 1. The instruments possess two separate spectrometers for the SWIR and TIR N_2O bands. The key instrument design parameters, including spectral coverage and spectral

resolution, are selected through iterative assessment of N_2O absorption strength and instrument performance using linear sensitivity analysis in concert with the current technology and industry standards for both airborne and spaceborne instruments. A Gaussian instrument spectral response function (ISRF) is assumed with a full width at half maximum (FWHM) spanning three spectral sampling intervals ($\mathrm{d}\lambda$). This corresponds to spectral resolutions of approximately 0.1725 nm (0.33 cm^{-1}) in the SWIR band for both airborne and spaceborne instruments. In the TIR band, the spectral resolutions are 0.90 nm (0.14 cm^{-1}) and 0.75 nm (0.12 cm^{-1}) for the airborne and spaceborne instruments, respectively. These spectral resolutions are within the range of existing and proposed trace-gas remote sensing instruments operating in the SWIR and TIR spectral regions (Bowman et al., 2006; Ricaud et al., 2021; Nakajima et al., 2012). In addition, a preliminary optical design assessment has been performed for the proposed TIR instrument, including the grating requirements and optical train. The grating is the component most strongly affected by the high spectral sampling, and a manufacturability assessment indicates high confidence that such a grating can be produced.

Due to limited space in the target aircraft, we choose smaller focal plane arrays (FPA) for the airborne instrument, which contain 1280×1024 pixels for the SWIR spectrometer and 640×512 pixels for the TIR spectrometer. The FPA dimension for the spaceborne instrument is 2048×2048 pixels for both bands. Due to the substantially smaller TIR focal plane array assumed for the airborne instrument relative to the spaceborne, a narrower TIR wavelength range is selected for the airborne case while maintaining the desired spectral performance. The along-track ground pixel size $\mathrm{d}y$ is determined by the ground speed of the platform v and the exposure time $\mathrm{d}t$ as $\mathrm{d}y = v\,\mathrm{d}t$. The swath width for the airborne instrument is about 2.5 km at a representative aircraft altitude of 9.25 km, and for the spaceborne instrument, about 320 km at an orbit height of 600 km. The native across-track ground pixel size, or ground sampling distance (GSD, denoted as $\mathrm{d}x_0$), reflects how the swath is sampled by the spatial dimension of the FPA, which at maximum contains 1024 SWIR and 512 TIR pixels for the airborne instrument and 2048 pixels for the spaceborne instrument. To collocate the footprints of two bands and make them square-like, the native across-track pixels are binned by a factor B, such that the final across-track ground pixel size $\mathrm{d}x$ is

$$\mathrm{d}x = B\,\mathrm{d}x_0. \tag{9}$$

The combination of SWIR and TIR spectra associated with a common ground footprint with dimension $\mathrm{d}x \times \mathrm{d}y$ is referred to as a "sounding" of N_2O. For further analysis of the detectability of X_{N_2O} variability, it is helpful to define a footprint size d_0 for an N_2O sounding as the edge size of a square having the same area of the ground footprint:

$$d_0 = \sqrt{\mathrm{d}x\,\mathrm{d}y}. \tag{10}$$

The observation error covariance matrix ($\mathbf{S_o}$) is assumed to be diagonal; in other words, the noise of individual detector pixels follows independent Gaussian distributions. The standard deviation of observation error is calculated by multiplying each single-channel radiance r with a signal-to-noise ratio (SNR):

$$\mathrm{SNR} = \frac{S}{N}, \tag{11}$$

Table 1. Instrument design parameters for airborne and spaceborne instruments.

Parameter	Symbol [unit]	Airborne SWIR	Airborne TIR	Spaceborne SWIR	Spaceborne TIR
Observation altitude	h_t [km]	9.25		600	
Swath width	[km]	2.5		320	
Exposure time	$\mathrm{d}t$ [s]	0.1		0.1	
Ground speed	v [m s^{-1}]	200		7010	
Along-track size	$\mathrm{d}y = v\,\mathrm{d}t$ [m]	20		701	
Across-track size	$\mathrm{d}x = B\,\mathrm{d}x_0$ [m]	20		640	
Footprint size	$d_0 = \sqrt{\mathrm{d}x\,\mathrm{d}y}$ [m]	20		670	
Wavelength range	[nm]	2240–2300	7820–8000	2240–2300	7600–8000
Spectral sampling	$\mathrm{d}\lambda$ [nm]	0.0575	0.3	0.0575	0.25
Slit width[a]	$n_{sample} \times \mathrm{d}\lambda$ [nm]	~~3~~ 0.1725	~~3~~ 0.9	~~3~~ 0.1725	~~3~~ 0.75
Detector pixel size	$\mathrm{d}p$ [μm]	12	15	18	18
f-number	f	2	2	2	2
System efficiency	η	0.46	0.35	0.5	0.5
Readout noise	N_r [electrons]	210	200	60	60
Dark current	D [electrons s^{-1}]	1.8×10^5	7×10^6	100	100
GSD	$\mathrm{d}x_0$ [m]	2.5	5	160	160
Across-track binning	B	8	4	4	4

[a] ~~Gaussian slit function (i.e., instrument spectral response function, ISRF) is assumed~~FWHM of Gaussian ISRF.

where the signal S and noise N are measured by number of electrons. The signal is computed as

$$S = \frac{\pi}{4} \cdot r \cdot \frac{\mathrm{d}p^2}{f^2} \cdot n_{\text{sample}} \cdot \mathrm{d}\lambda \cdot \mathrm{d}t \cdot \eta, \tag{12}$$

where r is the observed radiance at a specific wavelength ($\mathrm{photons \cdot s^{-1} \cdot cm^{-2} \cdot nm^{-1} \cdot sr^{-1}}$), $\mathrm{d}p$ is detector pixel size, f is f-number, n_{sample} is slit width measured as the ratio between the full width at half maximum of the instrument spectral response function (ISRF) and the spectral sampling interval, $\mathrm{d}\lambda$, $\mathrm{d}t$ is exposure time, and η is system efficiency. All parameters except the radiance are listed in Table 1. The total noise per exposure is computed as the quadrature sum of readout noise (N_r) and shot noise, the latter having contributions from both the signal and the cumulative dark current (D) over the exposure time. Considering the across-track binning factor B, the noise for each sounding is

$$N = \sqrt{\frac{S + D\,\mathrm{d}t + N_r^2}{B}}. \tag{13}$$

Figure 5 (top row) shows the simulated radiance spectra of a ~~typical sounding~~ daytime clear-sky summertime sounding selected from the CrIS ensemble over the US Midwest, at the spectral ranges and resolutions of the spaceborne instrument,

with and without N_2O, ~~by~~ using the radiative transfer model detailed in section 3.1.4. The simulation assumes a a solar zenith angle (SZA) of 30°, nadir viewing geometry, representative SWIR grass surface albedo of 0.159, TIR surface emissivity of 0.98, surface temperature of 307.3 K and thermal contrast of 4.6 K from the selected CrIS sounding. The spectral resolutions of the simulated spectra are 0.1725 nm for the SWIR band and 0.75 nm for the TIR band, corresponding to three times the spectral sampling intervals. In the SWIR band, differences with and without N_2O are small, owing to weak absorption lines, whereas the TIR N_2O features are much more prominent. The other spectral lines are mostly due to CH_4 and H_2O absorption with minor contributions from solar Fraunhofer lines for the SWIR. Figure 5 (bottom row) shows the corresponding SNR estimates calculated using Eq. 11 for the spaceborne instrument. The SNR for the SWIR band is significantly lower than that for the TIR due to lower radiance levels and finer spectral sampling. The SNR for the airborne instrument (not shown) appears similar but is slightly lower due to higher readout noise.

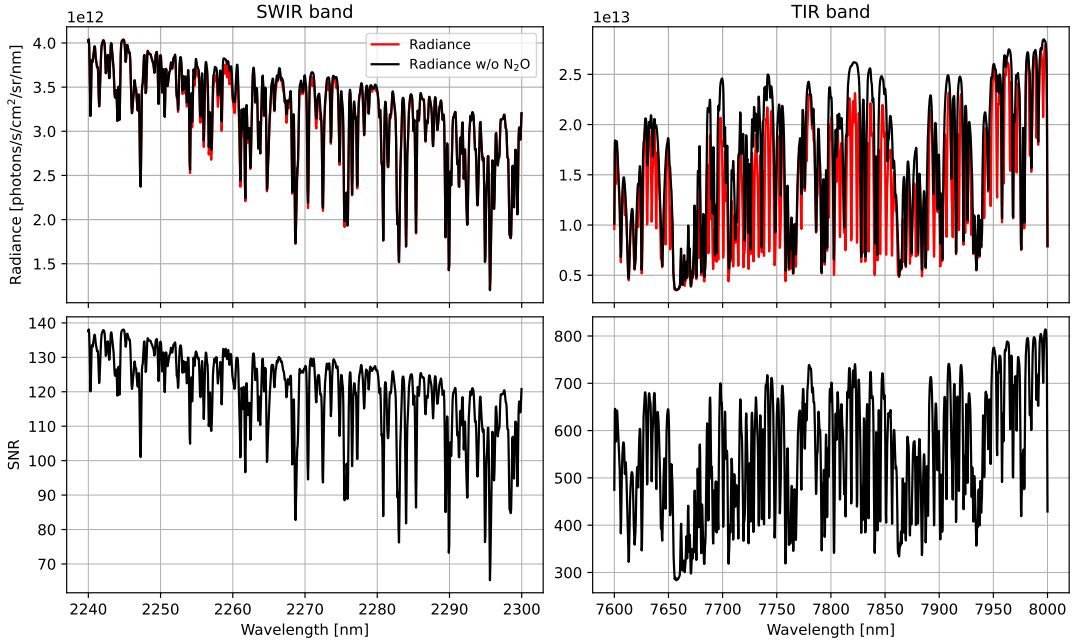

Figure 5. Top row shows simulated radiance spectra at the spectral ranges and resolutions of the spaceborne instrument, and bottom row shows corresponding signal-to-noise ratio (SNR). The left column shows the SWIR band (2240–2300 nm) with spectral resolution of 0.1725 nm, and the right column shows the TIR band (7600–8000 nm) with spectral resolution of 0.75 nm. In the top panels, the black curves represent simulated radiance with N_2O abundance set to zero, highlighting the absorption features attributable to N_2O. Radiance is expressed in units of $\mathrm{photons\,s^{-1}\,cm^{-2}\,nm^{-1}\,sr^{-1}}$. SWIR band shows weaker N_2O line strengths while the TIR band exhibits stronger absorption features and higher SNR due to strong signals.

3.1.4 Radiative transfer simulation

For radiative transfer, this study leverages the VLIDORT radiative transfer model (Spurr, 2006), a discrete-ordinate multiple scattering code for a stratified multi-layer atmosphere. The great advantage for the present N_2O application is VLIDORT's ability to generate not only radiances (in scalar mode without polarization) or (for polarized light calculations) Stokes 3-vectors, but also any group of analytically-calculated Jacobians with respect to any atmospheric profile variable (temperature and trace gas mixing ratios) and any surface quantity (e.g., albedo, temperature, and emissivity).

The SPLAT environment compiles atmospheric meteorological and constituent profiles, along with reference datasets to generate the linearized inputs required by VLIDORT to simulate both radiance and analytically derived Jacobian with respect to atmospheric state variables. For gases, the input absorption cross sections are based on look-up tables derived from HITRAN 2020 (Gordon et al., 2022), while aerosol optical properties are represented using Mie and T-matrix calculation. For more on these setups and specific use on MethaneAIR retrieval, see Spurr and Christi (2014) and Chan Miller et al. (2024).

Although more widely used in radiative transfer of solar radiations (e.g., Liu et al., 2010; O'Dell et al., 2012), VLIDORT can operate in both solar and thermal regimes and has been used in joint ultraviolet-TIR ozone retrieval from separate instruments (Cuesta et al., 2013). In the thermal regime, VLIDORT's radiative transfer is driven by blackbody thermal emission, treated in the atmosphere as a piecewise-continuous linear function of layer optical thickness. VLIDORT ingests a set of Planck functions, specified for the atmosphere at all layer boundaries, and again at the surface. Thermal emission is unpolarized and is assumed isotropic. The Planck functions at layer boundaries are linearized in order to determine temperature-profile Jacobian contributions additional to those arising from the temperature dependencies in the optical thicknesses (Spurr and Christi, 2019). This study marks the first application of the SPLAT-VLIDORT framework on the joint solar and thermal radiative transfer of the same instrument. All radiative transfer simulations are performed on a 19-layer pressure grid extending from the surface to the top of atmosphere. The simulations use a solar zenith angle of 30°, viewing zenith angle of 0° and assume clear-sky conditions using the SPLAT–VLIDORT radiative transfer model and HITRAN2020 spectroscopy. Surface emissivity from CrIS L2 product is used for TIR band and representative grass surface albedo from ASTER is used for SWIR band. The state vector include profiles of N_2O, CH_4, H_2O, and temperature, along with surface temperature.

Figure 6 shows the Jacobians of the SWIR (left column) and TIR bands (right column) with respect to atmospheric N_2O, CH_4, H_2O, and temperature profiles simulated by SPLAT-VLIDORT ~~over a typical Midwest summer environmental conditions~~ using profiles from a representative CrIS sounding and HITRAN2020 spectroscopy. The simulation conditions are same as described for Fig. 5 in Section 3.1.3. These Jacobians are calculated using the 19-layer atmospheric pressure grid, convolved with the ISRF and sampled at the spectral intervals of the spaceborne instrument specified in Table 1. Each panel represents a matrix, quantifying the change in observed radiance due to a unit perturbation in the state variable at given pressure level and wavelength. For N_2O (Fig. 6a-b), the SWIR band exhibits weak absorption but relatively uniform sensitivity throughout the column, while the TIR band provides stronger sensitivity in the mid- and upper troposphere, but less near-surface response. This complementary behavior reinforces the benefit of combining SWIR and TIR observations for improved N_2O retrievals.

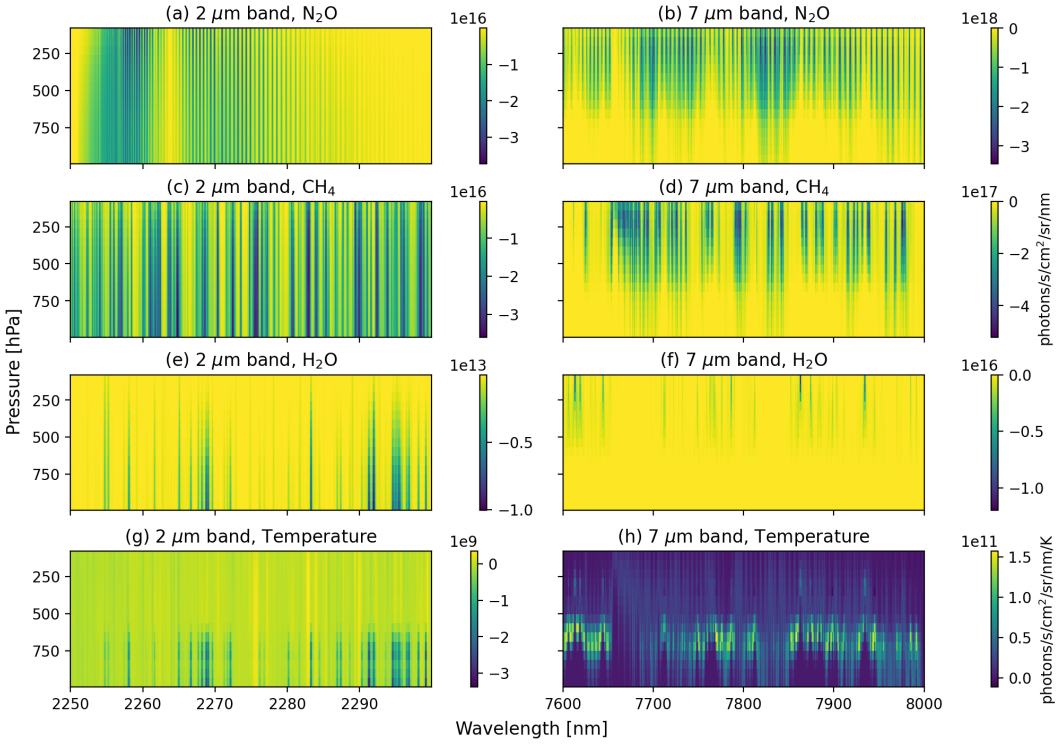

Figure 6. Jacobians with respect to N_2O, CH_4, H_2O, and temperature profiles for SWIR (a,c,e,g) and TIR (b,d,f,h) bands respectively. Each panel shows the sensitivity of observed radiance to a unit perturbation in the corresponding state variable as a function of pressure and wavelength. Only altitudes up until 100 hPa are shown to emphasize the troposphere and lower stratosphere, where most N_2O variability occurs. The distinct vertical sensitivity patterns between SWIR and TIR bands highlight their complementary roles in N_2O remote sensing.

3.2 Detectability of X_{N_2O} variability at different spatial scales

When spatially aggregating X_{N_2O} observations, the measurement error component propagated linearly from detector noise decreases with the target length scale d, ~~assuming independent sounding errors:~~ . This relationship assumes that the detector noise between individual soundings is independent and uncorrelated.

$$\sigma_{X_{N_2O}}(d) = \sigma_{X_{N_2O}}(d_0)\frac{d_0}{d}, \tag{14}$$

where $\sigma_{X_{N_2O}}(d_0)$ is the native measurement error at sounding footprint size d_0, obtained from the linear sensitivity analysis (Section 3.1). At a length scale $d \geq d_0$, it is meaningful to compare the aggregated measurement error $\sigma_{X_{N_2O}}(d)$ with the real-world X_{N_2O} variability $\delta_{X_{N_2O}}(d)$. With a known X_{N_2O} spatial distribution, its spatial variability can be quantified through a semivariogram (Metheron, 1963; Souri et al., 2022):

$$\delta_{X_{N_2O}}(d) = \sqrt{\frac{1}{2}\langle(\Delta_d X_{N_2O})^2\rangle}, \tag{15}$$

where $\delta_{X_{N_2O}}(d)$ is the standard deviation that represents variability at length scale d. Δ_d is an operator that differentiates all X_{N_2O} values separated by distances in a range of $d \pm \varepsilon$, where ε controls the granularity of the distance binning. The angular brackets $\langle\rangle$ average all point pairs within the specified bin.

In reality, spatially distributed X_{N_2O} measurements that can support semivariogram calculation are very rare. Nonetheless, we can approximate the semivariogram of X_{N_2O} using the semivariogram of in situ measured N_2O mixing ratio in the PBL:

$$\Delta_d X_{N_2O} = \frac{1-\exp(-h_b/H)}{1-\exp(-h_t/H)} \Delta_d \mu_{N_2O}, \tag{16}$$

where h_b is PBL height, h_t is observation altitude ~~as~~ determined by the instrument design parameters listed in Table 1 ~~,~~and $H = 7.5$ km is the assumed atmospheric scale height~~, and~~ . $\Delta_d \mu_{N_2O}$ is the spatial differentiation of PBL N_2O mixing ratio ~~,~~ ~~denoted as~~ between observation pairs separated by distance d, where μ_{N_2O} represents the in situ measurements collected along horizontal flight legs within the well-mixed PBL. Because h_t is significantly larger than h_b, the variability of X_{N_2O} is smaller than that of μ_{N_2O}. Equation 16 holds when the variability of X_{N_2O} is dominantly driven by the variability in the PBL, and the PBL N_2O mixing ratio is approximately uniform in the vertical direction. Combining Eq. 15 and 16, we obtain:

$$\delta_{X_{N_2O}}(d) = \frac{1-\exp(-h_b/H)}{1-\exp(-h_t/H)} \sqrt{\frac{1}{2}\langle(\Delta_d \mu_{N_2O})^2\rangle}. \tag{17}$$

Here, the semivariogram is directly calculated from extensively measured ~~PBL~~ N_2O mixing ratios (μ_{N_2O}) along horizontal flight legs within the well-mixed PBL during the MAIZE campaign, and the PBL height is inferred from collocated spiral profiles ~~. The~~ by identifying the sharp vertical transition of trace gases, temperature, and relative humidity between the well-mixed boundary layer and the free troposphere (Zhang et al., 2020). The X_{N_2O} variabilities calculated using Eq 17 differ between the airborne and spaceborne instruments because they sample different portions of the atmospheric column due to their different observational height (h_t). The semivariograms are calculated for each flight from 0 to 50 km with 0.25 km bin width.

Since X_{N_2O} measurement error decreases with d (Eq. 14), and X_{N_2O} variability typically increases with d (Eq. 17), a critical spatial scale for variability can be numerically solved from the following equation:

$$q \times \sigma_{X_{N_2O}}(d^*) = \delta_{X_{N_2O}}(d^*), \tag{18}$$

where q is a positive scalar. The solution $d^*(q)$ is the aggregated spatial scale beyond which X_{N_2O} variability exceeds q times the measurement error. $q = 1$ means the variability equals the measurement error, and $q = 2$ means the variability is twice the measurement error, which is typically assumed as the threshold of detectability (Jacob et al., 2016).

3.3 Detectability of N_2O emissions at different spatial scales

A complimentary way of understanding N_2O detectability is to characterize the critical spatial scales of detectable N_2O emission sources. Here, we adopt the approach from Jacob et al. (2016) for CH_4 detectability. Similar to Section 3.2, we aim to determine a critical spatial scale for emission, $d^+(q, E)$, beyond which the X_{N_2O} enhancement due to emissions at value E is q times the measurement error.

Assuming a uniform emission flux E and wind speed U, the enhancement of N_2O column amount due to emission at aggregated spatial scale d is

$$\Delta\Omega = \frac{Ed}{U}. \tag{19}$$

The N_2O enhancement increases with emission intensity and accumulating distance and decreases with wind speed. We assume $U = 5$ km h^{-1} following Jacob et al. (2016). At the same length scale d, the measurement error of the observable column amount, σ_Ω, can be derived from Eq. 14 by converting X_{N_2O} to a column amount:

$$\sigma_\Omega = \sigma_{X_{N_2O}} \frac{p_s(1-\exp(-h_t/H))}{Mg} \frac{d_0}{d}, \tag{20}$$

where p_s is surface pressure assumed to be 1000 hPa, M is air molar weight, and g is gravity and H is the assumed atmospheric scale height. The single-sounding measurement error $\sigma_{X_{N_2O}}$ (at d_0, notation dropped for simplicity), sounding footprint size d_0, and observation altitude h_t are inherent properties of the instrument. h_t is the only vertical parameter in this formulation and is used to determine the vertical extent of the atmospheric column observed by the instrument. Other parameters in Eq. 19 and 20 can be held constant except emission E and aggregation length scale d. Then, the detectability metric q can be calculated by dividing Eq. 19 and 20:

$$\begin{aligned} q(E,d) &= \frac{\Delta\Omega}{\sigma_\Omega} \\ &= \frac{Ed^2Mg}{U\sigma_{X_{N_2O}} d_0 p_s (1-\exp(-h_t/H))}. \end{aligned} \tag{21}$$

Equation 21 indicates that q increases linearly with emission, E, and quadratically with length scale, d, consistent with the intuition that more intensive and expansive emission sources are easier to detect. Alternatively, we can fix q to a certain value, e.g., 1 or 2, and solve for the critical length scale for emission level E:

$$d^+(q,E) = \sqrt{\frac{qU\sigma_{X_{N_2O}} d_0 p_s (1-\exp(-h_t/H))}{EMg}}. \tag{22}$$

4 Results

This section presents the outcomes of the linear sensitivity analysis and detectability methods introduced in the Section 3. Section 4.1 presents the dependence of X_{N_2O} measurement error and vertical sensitivity on spectral bands, observing platform properties, and a priori constraint strength. Section 4.2 uses semivariogram-based analysis to quantify the critical spatial scales at which natural X_{N_2O} variability becomes distinguishable from random measurement error. Section 4.3 relates emission strength, X_{N_2O} measurement error, and X_{N_2O} enhancement, providing a quantitative assessment of the critical spatial scales at which surface N_2O emissions can be resolved by the proposed instruments.

4.1 X_{N_2O} measurement error and vertical sensitivity by airborne and spaceborne instruments

We evaluate the effectiveness of airborne and spaceborne instruments in retrieving X_{N_2O} by analyzing their measurement error and vertical sensitivity. The measurement error is calculated using Eq. 6 and vertical sensitivity is calculated using Eq. 8.

Both metrics reflect the combined effect of observational constraint imposed by the instrument design and a priori constraint, as detailed in Section 3.1. Figure 7 illustrates the dependence of X_{N_2O} measurement error and near-surface sensitivity on the strength of a priori constraint for airborne and spaceborne instruments specified in Table 1 and compare results of three spectral settings; SWIR-only, TIR-only and joint SWIR–TIR setting. The near-surface sensitivity here is defined as the mean averaging kernel value of the lowest two atmospheric layers, representing the lowest $\sim$ 1 km of the atmosphere (corresponding pressure values are 962 and 901 hPa). In Fig. 7 the a priori constraint is adjusted by scaling the GOSAT/MethaneSAT-based N_2O prior standard deviation profile (see Fig. 4a) by a factor γ~~in the range of 0.03 to 10. The said range of~~.

The sensitivity analysis is performed using logarithmically spaced γ ~~span~~ values between 0.03 and 10, spanning retrieval regimes from strong domination by the prior regularization (small γ) to those controlled primarily by the ~~observations~~ observation constraint (large γ). The applied γ only modulates N_2O a priori covariance matrix and does not affect the a priori covariance matrices of all other state vector elements. The results presented in Fig. 7 are the mean values ~~from~~ calculated separately using the environmental conditions at 100 CrIS sounding locations shown in Fig. 1. These results correspond to single-shot observations at native instrument footprint size ($d_0 = 20$ m for airborne and $d_0 = 0.7$ km for spaceborne). Across the 100 selected CrIS soundings, the surface temperature ranges from 302.8 to 318.8 K (mean: 308.8 K), while the thermal contrast ranges from 2.8 to 12.3 K (mean: 6.6 K). Consistent across instruments and spectral settings, X_{N_2O} precision generally improves with tighter a priori constraint at small γ at the expense of degrading near-surface sensitivity.

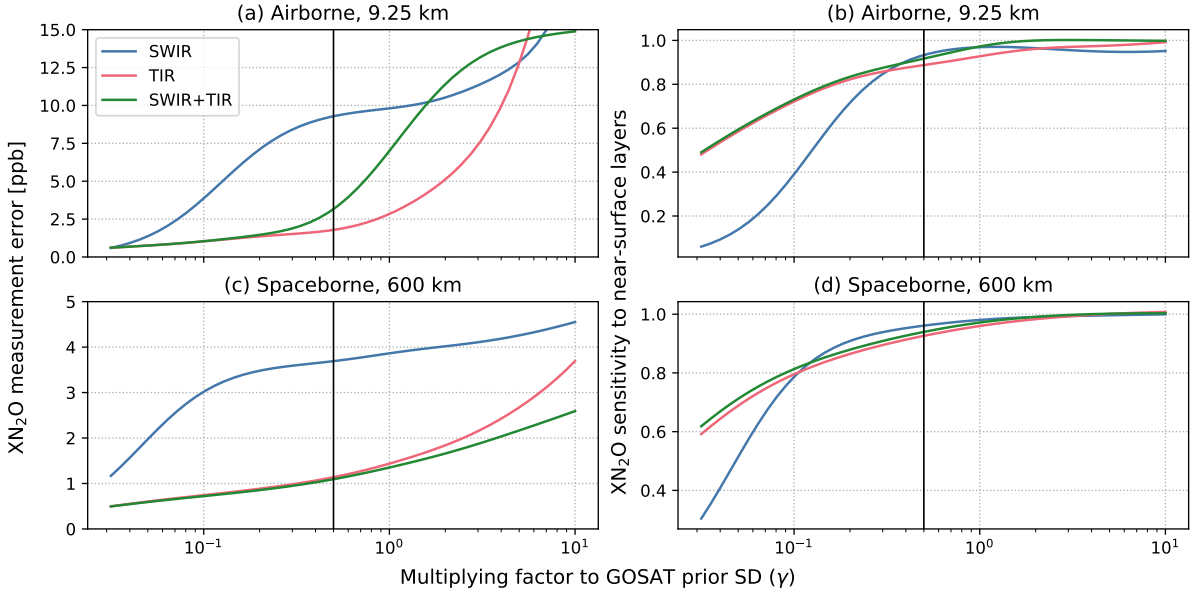

Figure 7. X_{N_2O} measurement error (left panels) and near-surface sensitivity quantified by the PBL mean of column averaging kernel (right panels) as a function of the a priori constraint strength (γ) applied to the N_2O prior standard deviation shown in Fig. 4a. Panels (a–b) correspond to the performance of the airborne instrument and panels (c–d) represent the performance of the spaceborne instrument. Each panel compares three spectral settings: SWIR-only (blue), TIR-only (pink), and combined SWIR–TIR (green) bands. Results are averaged over 100 CrIS soundings. The dual-band case achieves an optimal trade-off between near-surface sensitivity and X_{N_2O} measurement error at moderate strength of $\gamma = 0.5$ by balancing the observational and a priori constraint for both remote sensing platforms.

For the airborne instrument (Fig. 7a-b), the X_{N_2O} measurement error shown in panel (a) reveals three distinct regimes. In the rightmost side with large γ, the retrieval is largely dependent on the amount of information provided by observations, with random detector noise dominating the error. In this regime, SWIR–TIR joint setting delivers the lowest measurement error as it combines information from two bands which increase the effective observational constraint. In contrast, the SWIR and TIR bands alone have fewer ~~observations~~spectrum data points and thus provide weaker observation constraints than the joint band case, leading to larger errors. In a transition regime where γ is roughly 2–5, dual-band case briefly exhibit higher measurement errors than those from the SWIR or TIR bands alone, because the retrieval is less stabilized by the a priori constraint as compared to the single-band cases. In other words, SWIR-only and TIR-only cases begin to "feel" the a priori constraint earlier due to weaker observational constraints. As γ continues decreasing, all three cases become increasingly controlled by the a priori constraint, so the errors converge and the dual-band case falls between the SWIR-only and TIR-only cases. For the SWIR-only case, this transition to a prior-dominated regime is particularly abrupt, resulting in a rapid reduction in the X_{N_2O} measurement error that is synchronized with the simultaneous decrease in near-surface sensitivity. This behavior is also consistent with prior covariance tuning behavior reported for SWIR CH_4 retrievals in Chan Miller et al. (2024) and likely

reflects the inherent differences between shortwave and longwave radiative transfer, including both the strength and vertical distribution of the N_2O Jacobians.

Panel (b) highlights the trade-off value of γ between measurement error and near-surface sensitivity. At a very large γ (rightmost side) the retrieval is primarily observation dominated, resulting in relatively strong TIR near-surface sensitivity due to the stronger TIR observational constraint. Under this regime, the SWIR-only retrieval exhibits the weakest near-surface sensitivity, while the joint SWIR–TIR retrieval benefits from complementary information from both bands and therefore shows the highest sensitivity. A very strong prior (leftmost side, small γ) suppresses the SWIR near-surface information which increases rapidly as the prior is relaxed and then reaches a plateau. A value of $\gamma = 0.5$ (vertical black line) provides a balanced operating point because it sits on this plateau and SWIR near-surface sensitivity at this point is nearly saturated without entering the weak-prior regime where its value degrades quickly. This choice also keeps the dual-band case sensitive to observations in both bands, resulting in low measurement error while retaining sensitivity to the near-surface layers.

For the spaceborne instrument (Fig. 7c-d), the same qualitative order holds but the curves are less structured. X_{N_2O} measurement error (Fig. 7c) is overall lower than that from the airborne instrument largely due to the significantly wider TIR spectral range enabled by the spaceborne detector. The SWIR produces the largest measurement errors across all prior strengths. Both TIR-only and joint SWIR–TIR settings achieve comparable errors, but the integrated approach improves near-surface sensitivity relative to the TIR band alone (Fig. 7d). This added sensitivity is particularly beneficial given the inherently reduced surface sensitivity in satellite observations due to greater path lengths. We choose the same value of $\gamma = 0.5$ for the spaceborne instrument because it provides a balanced operating point between observational and a priori constraint with retaining sensitivity to near-surface layers along with achieving low X_{N_2O} measurement error. At this selected operating point γ, single sounding X_{N_2O} measurement error for the joint SWIR–TIR retrieval spans the interval 2.8–3.8 ppb (mean: 3.2 ppb) for the airborne instrument at a footprint size of $d_0 = 20$ m, whereas that for the spaceborne instrument ranges 0.6–1.8 ppb (mean: 1.1 ppb) at d_0 of 0.7 km.

Figure 8 shows the vertical structure of the N_2O column averaging kernel for three spectral settings under different a priori strengths, illustrating how measurement information is spread throughout the observed atmospheric column. For the airborne instrument (Fig. 8a–c), the SWIR-only exhibits stronger sensitivity to the column with a discontinuity at the observation altitude of 9.25 km . This behavior follows the solar-backscattered nature of the viewing geometry where the incident sunlight samples the atmosphere only once above the aircraft, whereas the photons traverse the air mass twice (downward to the surface and then upward to the sensor) below the aircraft. In contrast, the TIR-only relies on thermal emissions and therefore show no sensitivity above the aircraft altitude, with its response confined to layers below 9.25 km. Within this region, TIR band shows an enhanced sensitivity in the layers just below the aircraft, which is plausibly related to the vertical weighting function in the retrieval. The joint SWIR–TIR setting alleviates this localized amplification and distributes the information more evenly by integrating complementary strengths of both bands.

For the spaceborne instrument (Fig. 8d–f), the overall vertical patterns are similar but smoother, because satellite geometry at orbital altitude avoids the discontinuity that appears in the case of airborne instrument. SWIR-only setting maintains strong column-wide sensitivity approaching near-unity kernel values for sufficiently relaxed a priori constraints. The TIR-only and

the joint SWIR–TIR settings exhibit similar vertical response structures broadly, owing to the dominant contribution from the TIR band. Nevertheless, the inclusion of the SWIR band provides a visible improvement over the TIR-only case, particularly in enhancing sensitivity in the PBL, thereby highlighting the advantage of SWIR and TIR synergy for X_{N_2O} retrievals. For both instruments and all spectral settings, as the a priori constraint is relaxed (increasing γ), the averaging kernels start incorporating information from the observational constraint and shift from prior-dominated to measurement-informed.

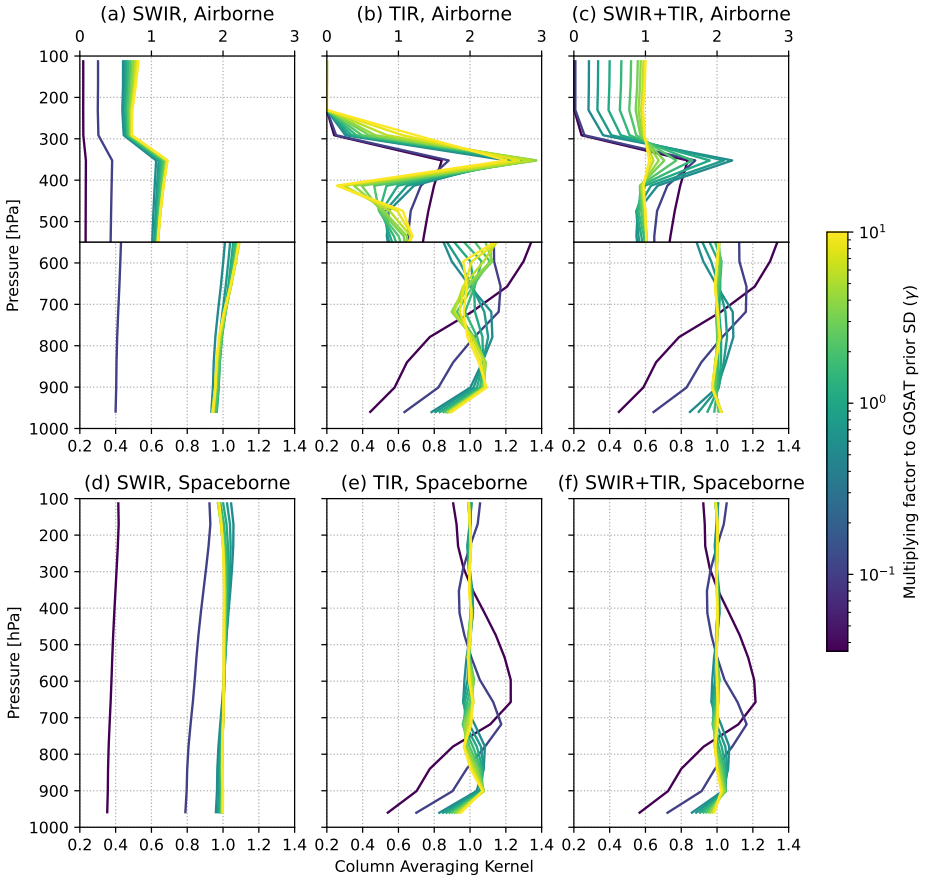

Figure 8. Column averaging kernels for N_2O retrievals using the SWIR-only (a, d), TIR-only (b, e), and joint SWIR–TIR (c, f) setting as a function of the a priori constraint strength (γ) applied to N_2O prior standard deviation shown in Fig. 4a. Panels (a–c) show results for the airborne instrument at 9.25 km observational altitude, and (d–f) show results for the spaceborne instrument at 600 km.

4.2 Spatial scales of detectable X_{N_2O} variability

We determine the critical spatial scales for the airborne and spaceborne instruments at which X_{N_2O} variability becomes distinguishable from measurement error. Here, the observed spatial structure of X_{N_2O} variability is inferred from in situ PBL

N_2O observations, and the instrument-specific X_{N_2O} measurement errors are estimated from the linear sensitivity analysis (see Section 3.2).

Figure 9 presents the semivariograms of PBL N_2O mixing ratios derived from eight MAIZE flights (i.e., $\frac{1}{2}\left\langle(\Delta_d \mu_{N_2O})^2\right\rangle$ in Eq. 17) along with their ensemble mean. Although the semivariance for all days generally increases with the separation distance, substantial variability is evident across individual flights. Several flights exhibit abrupt changes, which align with spatial intermittency in the PBL N_2O due to patchy sources and evolving boundary-layer conditions. The semivariogram sill, i.e., the maximum variance, also shows significant variation across flights, reflecting substantial differences in the overall intensity of heterogeneity. The extent of variability can also be attributed to meteorological conditions such as wind speed. Flights with stronger winds (e.g. 20220520, 20220521, 20220529, 20220530) show reduced semivariance as enhanced horizontal mixing diminishes spatial gradients, whereas flights with weaker winds (e.g. 20220518, 20220527) allow localized emission contrasts to persist, leading to higher semivariance. The ensemble-mean semivariogram, shown as the black line in Fig. 9, exhibits a smooth, steady rise and is utilized as a representative model of typical N_2O PBL variability for the subsequent detectability analysis.

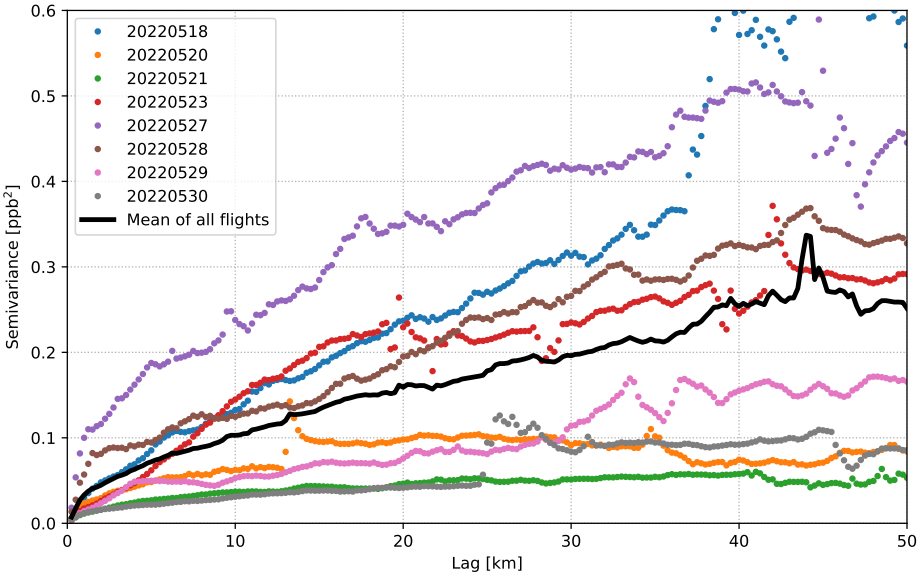

Figure 9. Semivariograms of PBL N_2O mixing ratios measured during the MAIZE campaign flights in 2022. Each colored line corresponds to a different flight date. The individual semivariograms reveal significant day-to-day variations likely due to heterogenetic nature of N_2O sources and localized meteorological conditions. The black line denotes the average semivariogram of all the flights, used as a representative model for quantifying critical spatial scales of detectable X_{N_2O} variability.

Built on the MAIZE semivariograms, the observed PBL N_2O variability translates to expected X_{N_2O} variability through Eq. 17 and is then compared with X_{N_2O} measurement error for airborne and spaceborne instruments. Measurement error here refers to the single-sounding uncertainty at the native footprint size d_0, whereas the uncertainty after averaging independent

soundings to the spatial aggregation scale d is referred to as X_{N_2O} precision. Figure 10 shows the trends of X_{N_2O} variability and X_{N_2O} precision as functions of the spatial aggregation scale (d). The two solid lines with circular markers in Fig. 10 represent the inferred X_{N_2O} variability for airborne (blue) and spaceborne (black) instruments, respectively. The circular markers represent the distance bins used in the semivariogram calculation. Although the same semivariogram is used in calculating the X_{N_2O} variability for both instruments, the results differ, as this variability depends on the observational altitude (h_t) of the instrument (see Eq. 17) and thus the relative weight of PBL variability in the observed atmospheric column. The higher h_t for the spaceborne instrument dilutes the boundary-layer heterogeneity more, yielding smaller X_{N_2O} variability as compared to that for airborne instrument at a given horizontal distance. The blue solid line in Fig. 10 corresponds to the aggregated precision $\sigma_{X_{N_2O}}(d)$ of airborne instrument, and black solid line corresponds to that of spaceborne instrument, computed from single-sounding X_{N_2O} measurement error ($\sigma_{X_{N_2O}}(d_0) = 3.2$ ppb for the airborne instrument and $\sigma_{X_{N_2O}}(d_0) = 1.1$ ppb for the spaceborne instrument) obtained in Section 4.1, using Eq. 14. Airborne and spaceborne precision lines do not overlap because $\sigma_{X_{N_2O}}(d_0)$ for airborne is larger (3.2 ppb) as compared to that for the spaceborne (1.1 ppb), and this quantity decreases quickly for the airborne instrument with the spatial averaging due to much smaller footprint size ($d_0 = 20$ m for airborne and $d_0 = 0.7$ km for spaceborne, see Table 1). As formulated in Eq. 14, the X_{N_2O} precision decreases log-linearly with d due to averaging of independent soundings, while the X_{N_2O} variability increases with d following the behavior shown in Fig. 9. The intersection points of these two quantities (marked with red stars in Fig. 10) define the critical spatial scale $d^*(q)$, at which atmospheric variability is q times the measurement error, as defined in Eq. 18. The dashed lines represent a more conservative detectability requirement by plotting $q \times \sigma_{X_{N_2O}}(d)$ with a commonly used criterion of $q = 2$. The corresponding intersection points locate the spatial scales where X_{N_2O} variability is twice the X_{N_2O} precision. For $q = 2$, the critical spatial scale ($d^*(q = 2)$) is approximately 2.5 km for the airborne and 22 km for the spaceborne instrument. This reflects how X_{N_2O} variability can be resolved from measurement noise under typical conditions observed during MAIZE.

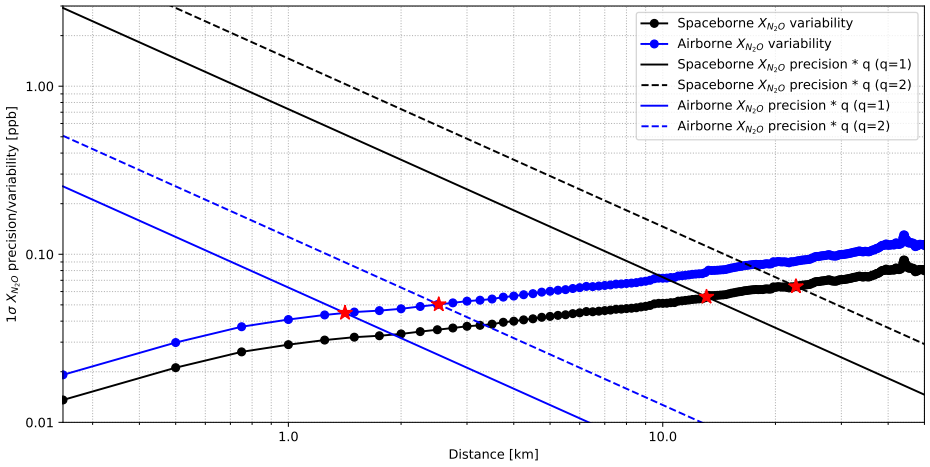

Figure 10. X_{N_2O} variability and X_{N_2O} precision for airborne (blue) and spaceborne (black) instruments. Solid lines with circular markers show X_{N_2O} variability derived from the MAIZE flights, ~~solid~~ where the circular markers indicate the semivariogram distance bins separated by 0.25 km. Solid and dashed straight lines represent aggregated X_{N_2O} precision multiplied by detectability thresholds of $q = 1$ and $q = 2$ respectively. The critical spatial scales $d^*(q)$, where the atmospheric variability become q times the precision, are indicated by red stars in the figure.

4.3 Spatial scales of detectable N_2O emissions

In Section 4.2, the critical spatial scales for variability are inferred by comparing X_{N_2O} precision against X_{N_2O} variability that implicitly reflects the influence of surface emissions, but this variability does not provide a quantitative mapping between N_2O emission strength and X_{N_2O} enhancements. Here, we make that connection explicit by modeling expected X_{N_2O} enhancement resulting from a uniform emission strength E and comparing it to the corresponding X_{N_2O} precision at matching spatial scales. We then quantify the emissions detectability using the $q(E, d)$ metric, introduced in Section 3.3. Here $q(E, d)$ is a continuous variable, defined as the ratio of emission-induced enhancement in X_{N_2O} to the aggregated measurement error at spatial aggregation scale d (Eq. 21). Figure 11 shows $q(E, d)$ as a function of emission strength (E) and spatial aggregation scale (d) as in Eq. 21 for the airborne (panel a) and spaceborne (panel b) instruments. Consistent across the instruments, detectability increases linearly with E and quadratically with d, implying that stronger sources can be detected at much finer scales while weaker emissions require substantial spatial aggregation to achieve the same level of confidence q.

White regions in Fig. 11 correspond to the detectability values below the minimum plotted contour level ($q < 2^{-8}$). The black contour lines in Fig. 11 indicate the solutions of Eq. 21 for $q = 1$ and $q = 2$; these provide a convenient way to read off the level of spatial aggregation needed to achieve a chosen detectability for a given emission strength. Here, $q = 1$ means that an emission-induced enhancement is equal to the aggregated precision and $q = 2$ indicates X_{N_2O} enhancement becomes twice the aggregated precision at a given spatial aggregation scale d. Using a representative uniform emissions of 5 nmol m^{-2} s^{-1}, consistent with the mean value of all nodes from 21–24 May in Fig. 3b, Fig. 11 implies critical spatial scale d^+ is ~ 2.1

km for the airborne instrument at $q = 1$ and ~ 2.9 km at $q = 2$. For the spaceborne instrument, the corresponding values are substantially larger with $d^+ \sim 8.4$ km at $q = 1$ and ~ 12 km at $q = 2$. For a higher uniform emissions of 10 nmol m^{-2} s^{-1}, the d^+ reduces to 1.5 km at $q = 1$ and 2.1 km at $q = 2$ for the airborne instrument, and the corresponding values decreases to 5.9 km ($q = 1$) and 8.5 km ($q = 2$) for the spaceborne instrument. d^+ values are different for airborne and spaceborne instruments as it is dependent on instrument properties such as footprint size (d_0), observational altitude (h_t) and single-sounding measurement error ($\sigma_{X_{N_2O}}(d_0)$). Overall, weaker emissions require larger-scale spatial aggregation to achieve a certain detectability level for both instruments.

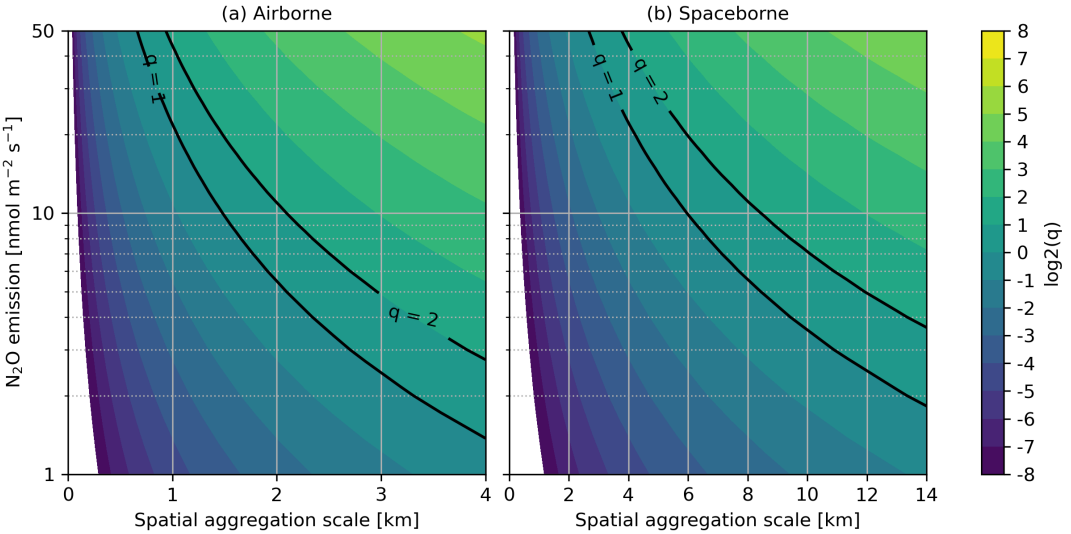

Figure 11. Detectability metric $q(E, d)$ as a function of emission strength (E) and spatial aggregation scale (d) for the (a) airborne and (b) spaceborne instruments. White regions indicate values below the minimum detectability threshold displayed in the plot ($q < 2^{-8}$). Solid black contours indicate $q = 1$ and $q = 2$, where the X_{N_2O} enhancements due to emission E are equal to and twice the aggregated measurement error at d, respectively. Instrument-specific measurement errors at d_0 are taken from linear sensitivity analysis. Stronger emissions can be resolved from noise at lower spatial scales while weaker emissions require more spatial aggregation.

4.4 Critical spatial scales of N_2O detection estimated using different approaches

This section provides a combined view of critical spatial scales reported as d^* and d^+ in Section 4.2 and 4.3, respectively. Table 2 summarizes these scales for the airborne and spaceborne instruments at two detectability levels, $q = 1$ and $q = 2$, illustrating how the required aggregation scale depends on detectability threshold and the approaches to estimate X_{N_2O} variability. In all cases, the airborne instrument consistently achieves smaller critical spatial scales as compared to spaceborne instrument. Although the airborne single-sounding error is larger, its much finer footprint size d_0 of 20 m allows more rapid reduction of random error with aggregation length scale d and detectability is achieved quickly under favorable conditions. In contrast, the spaceborne instrument with footprint size d_0 of 0.7 km, generally requires aggregation over several kilometers to reach

Table 2. Critical spatial scales at which X_{N_2O} signals become q times the aggregated measurement error for airborne and spaceborne instruments. Value are reported for $q = 1$ and $q = 2$.

Source of variability	Airborne critical spatial scale [km]		Spaceborne critical spatial scale [km]	
	$q = 1$	$q = 2$	$q = 1$	$q = 2$
Semivariogram (2022-05 average)	1.4	2.5	13	22
Semivariogram (2022-05-27)	0.92	1.7	9.4	16
$E = 1$ nmol m^{-2} s^{-1}	4.7	6.6	19	26
$E = 5$ nmol m^{-2} s^{-1}	2.1	2.9	8.4	12
$E = 10$ nmol m^{-2} s^{-1}	1.5	2.1	5.9	8.5
$E = 20$ nmol m^{-2} s^{-1}	1.1	1.5	4.2	5.9

the same detectability threshold, emphasizing that its strength lies in detecting broader regional patterns rather than localized enhancements.

For the variability-driven estimates, the choice of semivariogram primarily controls the inferred critical spatial scales. Using the mean semivariogram of all 8 flights conducted in May 2022 yields more conservative critical spatial scales than using the semivariogram of highest-variability flight (2022-05-27), which represents a more favorable scenario associated with relatively weak wind and reduced atmospheric mixing conditions. When the X_{N_2O} variability is twice the X_{N_2O} precision, d^* reduces from 2.5 km to 1.7 km for the airborne instrument and from 22 km to 16 km for the spaceborne instrument when switching from the mean semivariogram to the high-variability semivariogram. For the emission-driven cases, the critical spatial scales d^+ are reported for uniform emissions of $E = 1, 5, 10$ and 20 nmol m^{-2} s^{-1} in Table 2. As anticipated, d^+ decreases systematically with increasing uniform emission strength. For instance, increasing E from 1 to 20 nmol m^{-2} s^{-1}, reduces the $d^+(2, E)$ from 6.6 km to about 1.5 km for the airborne, and from 26 km to around 5.9 km for the spaceborne instrument. Together, the variability- and emission-driven results bracket the spatial scales over which X_{N_2O} signals are expected to become detectable under typical MAIZE-like boundary-layer variability and plausible agricultural emissions.

5 ~~Discussion~~ Summary and Conclusions

This study develops a practical and physically grounded framework to evaluate the capability of remote sensing instruments to detect atmospheric N_2O variability and column enhancements. To achieve this purpose, we expand the capacity of the SPLAT-VLIDORT radiative transfer model to jointly simulate solar-reflected (SWIR) and thermal-emitted (TIR) spectra within a unified framework. This framework provides a quantitative basis for assessing the combined observation from the SWIR and TIR bands under a priori regularization, with a particular emphasis on the trade-off between random measurement error and sensitivity to near-surface variability. A central consideration here is the use of X_{N_2O} measurement error, which is derived by linear propagation of Gaussian instrument noise. Although this represents only one component of the total error budget, it provides a lower bound on the achievable single-sounding error and therefore a first-order constraint for any N_2O-focused

mission. Also, in the error budget, measurement error is the only component that decreases predictably with spatial averaging of independent soundings, with the error scaling approximately as $1/\sqrt{N}$, where N is the number of independent soundings being aggregated. This relationship provides a direct link between single-sounding error and spatial aggregation scales required for resolving X_{N_2O} enhancements above the noise.

The linear sensitivity analysis further shows that the a priori constraint plays a decisive role in balancing observational and a priori contributions to the vertical distribution of information. A key methodological direction for future refinement is to move beyond a scaled prior covariance toward an ensemble covariance that will allow the regularization to be informed by physically plausible variability rather than an assumed scaling. Within the current setup, the joint SWIR–TIR setting balances the observational and a priori information contributions at a moderate prior strength by scaling N_2O prior standand deviation by 0.5. At this prior strength, dual-band case yields single-sounding measurement error of 3.2 ppb for the airborne instrument with 20 m footprint size and 1.1 ppb for the spaceborne instrument with 0.7 km footprint size, while preserving sensitivity to the near-surface layers.

An additional factor that could influence the performance is the presence of atmospheric aerosols. Aerosol scattering in the SWIR band modifies the photon path length and if not handled properly can introduce biases in the retrieved X_{N_2O}. Although, SPLAT–VLIDORT framework can incorporate aerosol optical properties, the scope of this study is limited to clear-sky condition. Future work should incorporate the influence of aerosol properties on X_{N_2O} accuracy, and how the SWIR and TIR bands can synergized to account for aerosol influences.

The instrument precision alone does not fix the detectability; rather, it is determined by how the instrument precision interacts with real-world X_{N_2O} variability. We therefore estimate the critical spatial scales of detection using two data-informed approaches that address different aspects of this problem and rely on distinct simplifying assumptions. First, the semivariogram-based analysis provides an empirical constraint on how X_{N_2O} variability grows with separation distance under realistic agricultural conditions sampled during the MAIZE campaign. Its main assumption is that X_{N_2O} variability is dominated by PBL variability and the PBL N_2O mixing ratio is approximately uniform in the vertical direction (Eq. 16-17). Second, the emission-based detectability metric $q(E, d)$ links emission strength and spatial aggregation scales to expected X_{N_2O} enhancements using an assumed wind speed of 5 km h^{-1}. The emission strengths considered are informed by the autochamber data shown in Fig. 3. These approaches are intended to provide first-order constraints rather than universal thresholds, and the inferred critical spatial scales should be interpreted as conditional on variability, emission strength, meteorology, and the chosen aggregation strategy.

Under MAIZE-like conditions, semivariogram-based analysis indicates that natural X_{N_2O} variability exceeds instrument precision at critical spatial scales of approximately 1–3 km for airborne and 10–23 km for spaceborne observations. Episodic agricultural emissions of 5 nmol m^{-2} s^{-1} require aggregation of measurement error to spatial scales of roughly 2–3 km for airborne and $\approx$ 8–12 km for spaceborne instrument to achieve required level of detection confidence. Together these results emphasize the complimentary roles of airborne and spaceborne observing platforms. Airborne instruments are best suited for resolving fine-scale heterogeneity associated with episodic emissions, whereas spaceborne observations can detect subtle column enhancements through spatial averaging while maintaining regional coverage. Overall, the combined SWIR–TIR band

concept for N_2O remote sensing introduced in this study addresses the longstanding limitations of SWIR and TIR bands alone, laying a foundation for future N_2O-focused missions by offering practical guidance for instrument design.

Code and data availability. The code related to linear sensitivity analysis can be accessed at https://github.com/Kang-Sun-CfA/Methane/l1/longwave.py

Author contributions. AR performed the analysis related to this study. KS developed the concept and linear sensitivity analysis framework. CCM contributed to the development of SPLAT. RS contributed to the development of VLIDORT. BB served as the primary contact for EDF funding and facilitated the project coordination. BDB, BMF, TUK, and NPL provided the information about instrument designs. KCP provided the CrIS data files to generate prior profiles. EAK provided MAIZE campaign flights data for semivariogram-based variability analysis. WCE, ERS, WHY provided autochambers N_2O flux data. AR and KS wrote and revised the paper. All authors contributed to the review of the paper.

Competing interests. The authors declare that they have no competing interests.

Acknowledgements. The authors acknowledge the Environmental Defense Fund for funding this project and the MethaneSAT science team for helpful discussion.

References

Ackett, R., Hilafu, H., Gelfand, I., and Saha, D.: Statistical Identification of Nitrous Oxide Hot Moments and Their Significance Across Global Agroecosystems, Journal of Geophysical Research: Biogeosciences, 130, e2025JG008 953, https://doi.org/https://doi.org/10.1029/2025JG008953, e2025JG008953 2025JG008953, 2025.

Adams, T. J., Plant, G., and Kort, E. A.: Deriving cropland N_2O emissions from space-based NO_2 observations, Atmospheric Chemistry and Physics, 26, 5517–5529, https://doi.org/10.5194/acp-26-5517-2026, 2026.

Barnet, C. D., Smith, N., Ide, K., Garrett, K., and Jones, E.: Evaluating the Value of CrIS Shortwave-Infrared Channels in Atmospheric-Sounding Retrievals, Remote Sensing, 15, https://doi.org/10.3390/rs15030547, 2023.

Bowman, K., Rodgers, C., Kulawik, S., Worden, J., Sarkissian, E., Osterman, G., Steck, T., Lou, M., Eldering, A., Shephard, M., Worden, H., Lampel, M., Clough, S., Brown, P., Rinsland, C., Gunson, M., and Beer, R.: Tropospheric emission spectrometer: retrieval method and error analysis, IEEE Transactions on Geoscience and Remote Sensing, 44, 1297–1307, https://doi.org/10.1109/TGRS.2006.871234, 2006.

Butz, A., Guerlet, S., Hasekamp, O., Schepers, D., Galli, A., Aben, I., Frankenberg, C., Hartmann, J.-M., Tran, H., Kuze, A., Keppel-Aleks, G., Toon, G., Wunch, D., Wennberg, P., Deutscher, N., Griffith, D., Macatangay, R., Messerschmidt, J., Notholt, J., and Warneke, T.: Toward accurate CO2 and CH4 observations from GOSAT, Geophysical Research Letters, 38, https://doi.org/10.1029/2011GL047888, 2011.

Chan Miller, C., Roche, S., Wilzewski, J. S., Liu, X., Chance, K., Souri, A. H., Conway, E., Luo, B., Samra, J., Hawthorne, J., Sun, K., Staebell, C., Chulakadabba, A., Sargent, M., Benmergui, J. S., Franklin, J. E., Daube, B. C., Li, Y., Laughner, J. L., Baier, B. C., Gautam, R., Omara, M., and Wofsy, S. C.: Methane retrieval from MethaneAIR using the CO_2 proxy approach: a demonstration for the upcoming MethaneSAT mission, Atmospheric Measurement Techniques, 17, 5429–5454, https://doi.org/10.5194/amt-17-5429-2024, 2024.

Chen, J., Viatte, C., Hedelius, J. K., Jones, T., Franklin, J. E., Parker, H., Gottlieb, E. W., Wennberg, P. O., Dubey, M. K., and Wofsy, S. C.: Differential column measurements using compact solar-tracking spectrometers, Atmospheric Chemistry and Physics, 16, 8479–8498, https://doi.org/10.5194/acp-16-8479-2016, 2016a.

Chen, Z., Griffis, T. J., Millet, D. B., Wood, J. D., Lee, X., Baker, J. M., Xiao, K., Turner, P. A., Chen, M., Zobitz, J., and Wells, K. C.: Partitioning N_2O emissions within the U.S. Corn Belt using an inverse modeling approach, Global Biogeochemical Cycles, 30, 1192–1205, https://doi.org/10.1002/2015GB005313, 2016b.

Chulakadabba, A., Sargent, M., Lauvaux, T., Benmergui, J. S., Franklin, J. E., Chan Miller, C., Wilzewski, J. S., Roche, S., Conway, E., Souri, A. H., Sun, K., Luo, B., Hawthrone, J., Samra, J., Daube, B. C., Liu, X., Chance, K., Li, Y., Gautam, R., Omara, M., Rutherford, J. S., Sherwin, E. D., Brandt, A., and Wofsy, S. C.: Methane point source quantification using MethaneAIR: a new airborne imaging spectrometer, Atmos. Meas. Tech., 16, 5771–5785, https://doi.org/10.5194/amt-16-5771-2023, aMT, 2023.

Connor, B., Bösch, H., McDuffie, J., Taylor, T., Fu, D., Frankenberg, C., O'Dell, C., Payne, V. H., Gunson, M., Pollock, R., Hobbs, J., Oyafuso, F., and Jiang, Y.: Quantification of uncertainties in OCO-2 measurements of XCO_2: simulations and linear error analysis, Atmospheric Measurement Techniques, 9, 5227–5238, https://doi.org/10.5194/amt-9-5227-2016, 2016.

Crisp, D.: Measuring atmospheric carbon dioxide from space with the Orbiting Carbon Observatory-2 (OCO-2), vol. 9607 of *SPIE Optical Engineering + Applications*, SPIE, https://doi.org/10.1117/12.2187291, 2015.

Crisp, D., Pollock, H. R., Rosenberg, R., Chapsky, L., Lee, R. A. M., Oyafuso, F. A., Frankenberg, C., O'Dell, C. W., Bruegge, C. J., Doran, G. B., Eldering, A., Fisher, B. M., Fu, D., Gunson, M. R., Mandrake, L., Osterman, G. B., Schwandner, F. M., Sun, K., Taylor,

T. E., Wennberg, P. O., and Wunch, D.: The on-orbit performance of the Orbiting Carbon Observatory-2 (OCO-2) instrument and its radiometrically calibrated products, Atmos. Meas. Tech., 10, 59–81, https://doi.org/10.5194/amt-10-59-2017, aMT, 2017.

Cuesta, J., Eremenko, M., Liu, X., Dufour, G., Cai, Z., Höpfner, M., von Clarmann, T., Sellitto, P., Foret, G., Gaubert, B., Beekmann, M., Orphal, J., Chance, K., Spurr, R., and Flaud, J.-M.: Satellite observation of lowermost tropospheric ozone by multispectral synergism of IASI thermal infrared and GOME-2 ultraviolet measurements over Europe, Atmospheric Chemistry and Physics, 13, 9675–9693, https://doi.org/10.5194/acp-13-9675-2013, 2013.

Dacic, N., Plant, G., and Kort, E. A.: Airborne Measurements Reveal High Spatiotemporal Variation and the Heavy-Tail Characteristic of Nitrous Oxide Emissions in Iowa, Journal of Geophysical Research: Atmospheres, 129, e2024JD041 403, https://doi.org/10.1029/2024JD041403, 2024.

Dils, B., De Mazière, M., Müller, J. F., Blumenstock, T., Buchwitz, M., de Beek, R., Demoulin, P., Duchatelet, P., Fast, H., Frankenberg, C., Gloudemans, A., Griffith, D., Jones, N., Kerzenmacher, T., Kramer, I., Mahieu, E., Mellqvist, J., Mittermeier, R. L., Notholt, J., Rinsland, C. P., Schrijver, H., Smale, D., Strandberg, A., Straume, A. G., Stremme, W., Strong, K., Sussmann, R., Taylor, J., van den Broek, M., Velazco, V., Wagner, T., Warneke, T., Wiacek, A., and Wood, S.: Comparisons between SCIAMACHY and ground-based FTIR data for total columns of CO, CH_4, CO_2 and N_2O, Atmospheric Chemistry and Physics, 6, 1953–1976, https://doi.org/10.5194/acp-6-1953-2006, 2006.

Eldering, A., Taylor, T. E., O'Dell, C. W., and Pavlick, R.: The OCO-3 mission: measurement objectives and expected performance based on 1-year of simulated data, Atmos. Meas. Tech., 12, 2341–2370, https://doi.org/10.5194/amt-12-2341-2019, aMT, 2019.

Feng, R. and Li, Z.: Current investigations on global N2O emissions and reductions: Prospect and outlook, Environmental Pollution, 338, 122 664, https://doi.org/10.1016/j.envpol.2023.122664, 2023.

Frankenberg, C., Sanghavi, S., Saha, A., Wennberg, P. O., Jacob, D. J., and Michalak, A. M.: On the Use of N_2O as a Light-Path Proxy for Accurate Greenhouse Gas Measurements From Space, Geophysical Research Letters, 52, e2024GL114 131, https://doi.org/https://doi.org/10.1029/2024GL114131, e2024GL114131 2024GL114131, 2025.

Gordon, I., Rothman, L., Hargreaves, R., Hashemi, R., Karlovets, E., Skinner, F., Conway, E., Hill, C., Kochanov, R., Tan, Y., Wcisło, P., Finenko, A., Nelson, K., Bernath, P., Birk, M., Boudon, V., Campargue, A., Chance, K., Coustenis, A., Drouin, B., Flaud, J., Gamache, R., Hodges, J., Jacquemart, D., Mlawer, E., Nikitin, A., Perevalov, V., Rotger, M., Tennyson, J., Toon, G., Tran, H., Tyuterev, V., Adkins, E., Baker, A., Barbe, A., Canè, E., Császár, A., Dudaryonok, A., Egorov, O., Fleisher, A., Fleurbaey, H., Foltynowicz, A., Furtenbacher, T., Harrison, J., Hartmann, J., Horneman, V., Huang, X., Karman, T., Karns, J., Kassi, S., Kleiner, I., Kofman, V., Kwabia–Tchana, F., Lavrentieva, N., Lee, T., Long, D., Lukashevskaya, A., Lyulin, O., Makhnev, V., Matt, W., Massie, S., Melosso, M., Mikhailenko, S., Mondelain, D., Müller, H., Naumenko, O., Perrin, A., Polyansky, O., Raddaoui, E., Raston, P., Reed, Z., Rey, M., Richard, C., Tóbiás, R., Sadiek, I., Schwenke, D., Starikova, E., Sung, K., Tamassia, F., Tashkun, S., Vander Auwera, J., Vasilenko, I., Vigasin, A., Villanueva, G., Vispoel, B., Wagner, G., Yachmenev, A., and Yurchenko, S.: The HITRAN2020 molecular spectroscopic database, Journal of Quantitative Spectroscopy and Radiative Transfer, 277, 107 949, https://doi.org/https://doi.org/10.1016/j.jqsrt.2021.107949, 2022.

Griffis, T. J., Hu, C., Baker, J. M., Wood, J. D., Millet, D. B., Erickson, M., Yu, Z., Deventer, M. J., Winker, C., and Chen, Z.: Tall Tower Ammonia Observations and Emission Estimates in the U.S. Midwest, Journal of Geophysical Research: Biogeosciences, 124, 3432–3447, https://doi.org/10.1029/2019JG005172, 2019.

Gvakharia, A., Kort, E. A., Smith, M. L., and Conley, S.: Evaluating Cropland N_2O Emissions and Fertilizer Plant Greenhouse Gas Emissions With Airborne Observations, Journal of Geophysical Research: Atmospheres, 125, e2020JD032 815, https://doi.org/https://doi.org/10.1029/2020JD032815, e2020JD032815 10.1029/2020JD032815, 2020.

Haszpra, L., Hidy, D., Taligás, T., and Barcza, Z.: First results of tall tower based nitrous oxide flux monitoring over an agricultural region in Central Europe, Atmospheric Environment, 176, 240–251, https://doi.org/10.1016/j.atmosenv.2017.12.035, 2018.

IPCC: Climate Change 2021: The Physical Science Basis, chap. 6, Cambridge University Press, https://www.ipcc.ch/report/ar6/wg1/, accessed June 2025, 2021.

Jacob, D. J., Turner, A. J., Maasakkers, J. D., Sheng, J., Sun, K., Liu, X., Chance, K., Aben, I., McKeever, J., and Frankenberg, C.: Satellite observations of atmospheric methane and their value for quantifying methane emissions, Atmospheric Chemistry and Physics, 16, 14 371–14 396, https://doi.org/10.5194/acp-16-14371-2016, 2016.

Jovani-Sancho, A. J., O'Reilly, P., Anshari, G., Chong, X. Y., Crout, N., Evans, C. D., Evers, S., Gan, J. Y., Gibbins, C. N., Gusmayanti, E., Jamaludin, J., Jaya, A., Page, S., Yosep, Y., Upton, C., Wilson, P., and Sjögersten, S.: CH4 and N2O emissions from smallholder agricultural systems on tropical peatlands in Southeast Asia, Global Change Biology, 29, 4279–4297, https://doi.org/10.1111/gcb.16747, 2023.

Kong, M., Mitu, F. F., Petersen, S. O., Lærke, P. E., Abalos, D., Sørensen, P., Brændholt, A., Bruun, S., Eriksen, J., and Dold, C.: A comparison of chamber-based methods for measuring N2O emissions from arable soils, Agricultural and Forest Meteorology, 370, 110 591, https://doi.org/10.1016/j.agrformet.2025.110591, 2025.

Kort, E. A., Patra, P. K., Ishijima, K., Daube, B. C., Jiménez, R., Elkins, J., Hurst, D., Moore, F. L., Sweeney, C., and Wofsy, S. C.: Tropospheric distribution and variability of N_2O: Evidence for strong tropical emissions, Geophysical Research Letters, 38, https://doi.org/10.1029/2011GL047612, 2011.

Kort, E. A., Gvakharia, A., Smith, M. L., Conley, S., and Frauhammer, K.: The 2017 Fertilizer Emissions Airborne Study (FEAST): Quantifying N_2O emissions from croplands and fertilizer plants in the Mississippi River Valley., in: AGU Fall Meeting Abstracts, vol. 2017, pp. B21H–03, 2017.

Liu, X., Bhartia, P. K., Chance, K., Spurr, R. J. D., and Kurosu, T. P.: Ozone profile retrievals from the Ozone Monitoring Instrument, Atmospheric Chemistry and Physics, 10, 2521–2537, https://doi.org/10.5194/acp-10-2521-2010, 2010.

Lorente, A., Borsdorff, T., Butz, A., Hasekamp, O., aan de Brugh, J., Schneider, A., Wu, L., Hase, F., Kivi, R., Wunch, D., Pollard, D. F., Shiomi, K., Deutscher, N. M., Velazco, V. A., Roehl, C. M., Wennberg, P. O., Warneke, T., and Landgraf, J.: Methane retrieved from TROPOMI: improvement of the data product and validation of the first 2 years of measurements, Atmos. Meas. Tech., 14, 665–684, https://doi.org/10.5194/amt-14-665-2021, aMT, 2021.

MacKay, K., Benmergui, J., Williams, J. P., Omara, M., Himmelberger, A., Sargent, M., Warren, J. D., Miller, C. C., Roche, S., Zhang, Z., Franklin, J., Guanter, L., Wofsy, S., and Gautam, R.: Assessment of methane emissions from US onshore oil and gas production using MethaneAIR measurements, Atmospheric Chemistry and Physics, 26, 1179–1192, https://doi.org/10.5194/acp-26-1179-2026, 2026.

Metheron, G.: Principles of geostatistics, economic geology, Economic Geology, 58, 1246–1266, 1963.

Molodovskaya, M., Singurindy, O., Richards, B. K., Warland, J., Johnson, M. S., and Steenhuis, T. S.: Temporal Variability of Nitrous Oxide from Fertilized Croplands: Hot Moment Analysis, Soil Science Society of America Journal, 76, 1728–1740, https://doi.org/https://doi.org/10.2136/sssaj2012.0039, 2012.

Murphy, R. M., Richards, K. G., Krol, D. J., Gebremichael, A. W., Lopez-Sangil, L., Rambaud, J., Cowan, N., Lanigan, G. J., and Saunders, M.: Assessing nitrous oxide emissions in time and space with minimal uncertainty using static chambers and eddy covariance from a temperate grassland, Agricultural and Forest Meteorology, 313, 108 743, https://doi.org/10.1016/j.agrformet.2021.108743, 2022.

Nakajima, M., Kuze, A., and Suto, H.: The current status of GOSAT and the concept of GOSAT-2, in: Sensors, Systems, and Next-Generation Satellites XVI, edited by Meynart, R., Neeck, S. P., and Shimoda, H., vol. 8533, p. 853306, International Society for Optics and Photonics, SPIE, https://doi.org/10.1117/12.974954, 2012.

Noël, S., Reuter, M., Buchwitz, M., Borchardt, J., Hilker, M., Schneising, O., Bovensmann, H., Burrows, J. P., Di Noia, A., Parker, R. J., Suto, H., Yoshida, Y., Buschmann, M., Deutscher, N. M., Feist, D. G., Griffith, D. W. T., Hase, F., Kivi, R., Liu, C., Morino, I., Notholt, J., Oh, Y. S., Ohyama, H., Petri, C., Pollard, D. F., Rettinger, M., Roehl, C., Rousogenous, C., Sha, M. K., Shiomi, K., Strong, K., Sussmann, R., Té, Y., Velazco, V. A., Vrekoussis, M., and Warneke, T.: Retrieval of greenhouse gases from GOSAT and GOSAT-2 using the FOCAL algorithm, Atmos. Meas. Tech., 15, 3401–3437, https://doi.org/10.5194/amt-15-3401-2022, aMT, 2022.

O'Dell, C. W., Connor, B., Bösch, H., O'Brien, D., Frankenberg, C., Castano, R., Christi, M., Eldering, D., Fisher, B., Gunson, M., McDuffie, J., Miller, C. E., Natraj, V., Oyafuso, F., Polonsky, I., Smyth, M., Taylor, T., Toon, G. C., Wennberg, P. O., and Wunch, D.: The ACOS CO_2 retrieval algorithm – Part 1: Description and validation against synthetic observations, Atmospheric Measurement Techniques, 5, 99–121, https://doi.org/10.5194/amt-5-99-2012, 2012.

Pan, D., Gelfand, I., Tao, L., Abraha, M., Sun, K., Guo, X., Chen, J., Robertson, G. P., and Zondlo, M. A.: A new open-path eddy covariance method for nitrous oxide and other trace gases that minimizes temperature corrections, Global Change Biology, 28, 1446–1457, https://doi.org/10.1111/gcb.15986, 2022.

Parker, R. J., Webb, A., Boesch, H., Somkuti, P., Barrio Guillo, R., Di Noia, A., Kalaitzi, N., Anand, J. S., Bergamaschi, P., Chevallier, F., Palmer, P. I., Feng, L., Deutscher, N. M., Feist, D. G., Griffith, D. W. T., Hase, F., Kivi, R., Morino, I., Notholt, J., Oh, Y.-S., Ohyama, H., Petri, C., Pollard, D. F., Roehl, C., Sha, M. K., Shiomi, K., Strong, K., Sussmann, R., Té, Y., Velazco, V. A., Warneke, T., Wennberg, P. O., and Wunch, D.: A decade of GOSAT Proxy satellite CH_4 observations, Earth System Science Data, 12, 3383–3412, https://doi.org/10.5194/essd-12-3383-2020, 2020.

Prather, M. J., Hsu, J., DeLuca, N. M., Jackman, C. H., Oman, L. D., Douglass, A. R., Fleming, E. L., and Strahan, S. E.: Measuring and modeling the lifetime of nitrous oxide including its variability, Journal of Geophysical Research: Atmospheres, 120, 5693–5705, https://doi.org/10.1002/2015JD023267, 2015.

Prather, M. J., Froidevaux, L., and Livesey, N. J.: Observed changes in stratospheric circulation: decreasing lifetime of N_2O, 2005–2021, Atmospheric Chemistry and Physics, 23, 843–849, https://doi.org/10.5194/acp-23-843-2023, 2023.

Rana, G., Vitale, D., Azzolini, A., Mastrangelo, M., Dyroff, C., Di Tommasi, P., Famulari, D., Alberici, A., and Ferrara, R. M.: Applicability of a closed-path analyser for simultaneous eddy covariance measurement of carbon dioxide, water vapor, nitrous oxide, methane, ozone and ammonia fluxes in a horticultural crop, Science of The Total Environment, 991, 179 900, https://doi.org/10.1016/j.scitotenv.2025.179900, 2025.

Ricaud, P., Attié, J.-L., Chalinel, R., Pasternak, F., Léonard, J., Pison, I., Pattey, E., Thompson, R. L., Zelinger, Z., Lelieveld, J., Sciare, J., Saitoh, N., Warner, J., Fortems-Cheiney, A., Reynal, H., Vidot, J., Brooker, L., Berdeu, L., Saint-Pé, O., Patra, P. K., Dostál, M., Suchánek, J., Nevrlý, V., and Zwaaftink, C. G.: The Monitoring Nitrous Oxide Sources (MIN2OS) satellite project, Remote Sensing of Environment, 266, 112 688, https://doi.org/10.1016/j.rse.2021.112688, 2021.

Rodgers, C. D.: Inverse methods for atmospheric sounding: theory and practice, vol. 2, World scientific, 2000.

Shrestha, N. K. and Wang, J.: Current and future hot-spots and hot-moments of nitrous oxide emission in a cold climate river basin, Environmental Pollution, 239, 648–660, https://doi.org/https://doi.org/10.1016/j.envpol.2018.04.068, 2018.

Smith, K. A.: Changing views of nitrous oxide emissions from agricultural soil: key controlling processes and assessment at different spatial scales, European Journal of Soil Science, 68, 137–155, https://doi.org/10.1111/ejss.12409, 2017.

Souri, A. H., Chance, K., Sun, K., Liu, X., and Johnson, M. S.: Dealing with spatial heterogeneity in pointwise-to-gridded-data comparisons, Atmospheric Measurement Techniques, 15, 41–59, https://doi.org/10.5194/amt-15-41-2022, 2022.

South, D. W.: Methane Emissions, Nowhere to Hide from Detection and Compliance Monitoring with Newly Launched Satellite, Climate and Energy, 40, 28–32, https://doi.org/10.1002/gas.22407, 2024.

Spurr, R.: VLIDORT: A linearized pseudo-spherical vector discrete ordinate radiative transfer code for forward model and retrieval studies in multilayer multiple scattering media, Journal of Quantitative Spectroscopy and Radiative Transfer, 102, 316–342, https://doi.org/10.1016/j.jqsrt.2006.05.005, 2006.

Spurr, R. and Christi, M.: On the generation of atmospheric property Jacobians from the (V)LIDORT linearized radiative transfer models, Journal of Quantitative Spectroscopy and Radiative Transfer, 142, 109–115, https://doi.org/https://doi.org/10.1016/j.jqsrt.2014.03.011, 2014.

Spurr, R. and Christi, M.: The LIDORT and VLIDORT Linearized Scalar and Vector Discrete Ordinate Radiative Transfer Models: Updates in the Last 10 Years, pp. 1–62, Springer International Publishing, Cham, ISBN 978-3-030-03445-0, https://doi.org/10.1007/978-3-030-03445-0_1, 2019.

Staebell, C., Sun, K., Samra, J., Franklin, J., Chan Miller, C., Liu, X., Conway, E., Chance, K., Milligan, S., and Wofsy, S.: Spectral calibration of the MethaneAIR instrument, Atmospheric Measurement Techniques, 14, 3737–3753, https://doi.org/10.5194/amt-14-3737-2021, 2021.

Stuchiner, E. R., Xu, J., Eddy, W. C., DeLucia, E. H., and Yang, W. H.: Hot or Not? An Evaluation of Methods for Identifying Hot Moments of Nitrous Oxide Emissions From Soils, Journal of Geophysical Research: Biogeosciences, 130, e2024JG008 138, https://doi.org/10.1029/2024JG008138, 2025.

Suto, H., Kataoka, F., Kikuchi, N., Knuteson, R. O., Butz, A., Haun, M., Buijs, H., Shiomi, K., Imai, H., and Kuze, A.: Thermal and near-infrared sensor for carbon observation Fourier transform spectrometer-2 (TANSO-FTS-2) on the Greenhouse gases Observing SATellite-2 (GOSAT-2) during its first year in orbit, Atmospheric Measurement Techniques, 14, 2013–2039, https://doi.org/10.5194/amt-14-2013-2021, 2021.

Syakila, A. and Kroeze, C.: The global nitrous oxide budget revisited, Greenhouse Gas Measurement and Management, 1, 17–26, https://doi.org/10.3763/ghgmm.2010.0007, 2011.

Taylor, T. E., O'Dell, C. W., Baker, D., Bruegge, C., Chang, A., Chapsky, L., Chatterjee, A., Cheng, C., Chevallier, F., Crisp, D., Dang, L., Drouin, B., Eldering, A., Feng, L., Fisher, B., Fu, D., Gunson, M., Haemmerle, V., Keller, G. R., Kiel, M., Kuai, L., Kurosu, T., Lambert, A., Laughner, J., Lee, R., Liu, J., Mandrake, L., Marchetti, Y., McGarragh, G., Merrelli, A., Nelson, R. R., Osterman, G., Oyafuso, F., Palmer, P. I., Payne, V. H., Rosenberg, R., Somkuti, P., Spiers, G., To, C., Weir, B., Wennberg, P. O., Yu, S., and Zong, J.: Evaluating the consistency between OCO-2 and OCO-3 XCO2 estimates derived from the NASA ACOS version 10 retrieval algorithm, Atmos. Meas. Tech., 16, 3173–3209, https://doi.org/10.5194/amt-16-3173-2023, aMT, 2023.

Thompson, R. L., Lassaletta, L., Patra, P. K., Wilson, C., Wells, K. C., Gressent, A., Koffi, E. N., Chipperfield, M. P., Winiwarter, W., Davidson, E. A., Tian, H., and Canadell, J. G.: Acceleration of global N2O emissions seen from two decades of atmospheric inversion, Nature Climate Change, 9, 993–998, https://doi.org/10.1038/s41558-019-0613-7, 2019.

Tian, H., Xu, R., Canadell, J. G., Thompson, R. L., Winiwarter, W., Suntharalingam, P., Davidson, E. A., Ciais, P., Jackson, R. B., Janssens-Maenhout, G., Prather, M. J., Regnier, P., Pan, N., Pan, S., Peters, G. P., Shi, H., Tubiello, F. N., Zaehle, S., Zhou, F., Arneth, A., Battaglia, G., Berthet, S., Bopp, L., Bouwman, A. F., Buitenhuis, E. T., Chang, J., Chipperfield, M. P., Dangal, S. R. S., Dlugokencky, E., Elkins, J. W., Eyre, B. D., Fu, B., Hall, B., Ito, A., Joos, F., Krummel, P. B., Landolfi, A., Laruelle, G. G., Lauerwald, R., Li, W., Lienert, S., Maavara, T., MacLeod, M., Millet, D. B., Olin, S., Patra, P. K., Prinn, R. G., Raymond, P. A., Ruiz, D. J., van der Werf, G. R., Vuichard,

N., Wang, J., Weiss, R. F., Wells, K. C., Wilson, C., Yang, J., and Yao, Y.: A comprehensive quantification of global nitrous oxide sources and sinks, Nature, 586, 248–256, https://doi.org/10.1038/s41586-020-2780-0, 2020.

Tian, H., Pan, N., Thompson, R. L., Canadell, J. G., Suntharalingam, P., Regnier, P., Davidson, E. A., Prather, M., Ciais, P., Muntean, M., Pan, S., Winiwarter, W., Zaehle, S., Zhou, F., Jackson, R. B., Bange, H. W., Berthet, S., Bian, Z., Bianchi, D., Bouwman, A. F., Buitenhuis, E. T., Dutton, G., Hu, M., Ito, A., Jain, A. K., Jeltsch-Thömmes, A., Joos, F., Kou-Giesbrecht, S., Krummel, P. B., Lan, X., Landolfi, A., Lauerwald, R., Li, Y., Lu, C., Maavara, T., Manizza, M., Millet, D. B., Mühle, J., Patra, P. K., Peters, G. P., Qin, X., Raymond, P., Resplandy, L., Rosentreter, J. A., Shi, H., Sun, Q., Tonina, D., Tubiello, F. N., van der Werf, G. R., Vuichard, N., Wang, J., Wells, K. C., Western, L. M., Wilson, C., Yang, J., Yao, Y., You, Y., and Zhu, Q.: Global nitrous oxide budget (1980–2020), Earth System Science Data, 16, 2543–2604, https://doi.org/10.5194/essd-16-2543-2024, 2024.

Tikkasalo, O. P., Peltola, O., Alekseychik, P., Heikkinen, J., Launiainen, S., Lehtonen, A., Li, Q., Martínez-García, E., Peltoniemi, M., Salovaara, P., Tuominen, V., and Mäkipää, R.: Eddy-covariance fluxes of CO2, CH4 and N2O in a drained peatland forest after clear-cutting, Biogeosciences, 22, 1277–1300, https://doi.org/10.5194/bg-22-1277-2025, bG, 2025.

Vandenbussche, S., Langerock, B., Vigouroux, C., Buschmann, M., Deutscher, N. M., Feist, D. G., García, O., Hannigan, J. W., Hase, F., Kivi, R., Kumps, N., Makarova, M., Millet, D. B., Morino, I., Nagahama, T., Notholt, J., Ohyama, H., Ortega, I., Petri, C., Rettinger, M., Schneider, M., Servais, C. P., Sha, M. K., Shiomi, K., Smale, D., Strong, K., Sussmann, R., Té, Y., Velazco, V. A., Vrekoussis, M., Warneke, T., Wells, K. C., Wunch, D., Zhou, M., and De Mazière, M.: Nitrous Oxide Profiling from Infrared Radiances (NOPIR): Algorithm Description, Application to 10 Years of IASI Observations and Quality Assessment, Remote Sensing, 14, https://doi.org/10.3390/rs14081810, 2022.

Waldmann, P., Eckl, M., Knez, L., Gottschaldt, K.-D., Fiehn, A., Mallaun, C., Gałkowski, M., Kiemle, C., Hutjes, R., Röckmann, T., Chen, H., and Roiger, A.: Quantifying agricultural N_2O and CH_4 emissions in the Netherlands using an airborne eddy covariance system, Atmospheric Measurement Techniques, 19, 185–210, https://doi.org/10.5194/amt-19-185-2026, 2026.

Warren, J. D., Sargent, M., Williams, J. P., Omara, M., Miller, C. C., Roche, S., MacKay, K., Manninen, E., Chulakadabba, A., Himmelberger, A., Benmergui, J., Zhang, Z., Guanter, L., Wofsy, S., and Gautam, R.: Sectoral contributions of high-emitting methane point sources from major US onshore oil and gas producing basins using airborne measurements from MethaneAIR, Atmospheric Chemistry and Physics, 25, 10 661–10 675, https://doi.org/10.5194/acp-25-10661-2025, 2025.

Weber, J., Keeble, J., Abraham, N. L., Beerling, D. J., and Martin, M. V.: Global agricultural N2O emission reduction strategies deliver climate benefits with minimal impact on stratospheric O3 recovery, npj Climate and Atmospheric Science, 7, 121, https://doi.org/10.1038/s41612-024-00678-2, 2024.

Wilkerson, J., Dobosy, R., Sayres, D. S., Healy, C., Dumas, E., Baker, B., and Anderson, J. G.: Permafrost nitrous oxide emissions observed on a landscape scale using the airborne eddy-covariance method, Atmospheric Chemistry and Physics, 19, 4257–4268, 2019.

Worden, H. M., Deeter, M. N., Edwards, D. P., Gille, J. C., Drummond, J. R., and Nédélec, P.: Observations of near-surface carbon monoxide from space using MOPITT multispectral retrievals, Journal of Geophysical Research: Atmospheres, 115, https://doi.org/https://doi.org/10.1029/2010JD014242, 2010.

Xiang, B., Miller, S. M., Kort, E. A., Santoni, G. W., Daube, B. C., Commane, R., Angevine, W. M., Ryerson, T. B., Trainer, M. K., Andrews, A. E., Nehrkorn, T., Tian, H., and Wofsy, S. C.: Nitrous oxide (N_2O) emissions from California based on 2010 CalNex airborne measurements, Journal of Geophysical Research: Atmospheres, 118, 2809–2820, https://doi.org/10.1002/jgrd.50189, 2013.

Xiong, X., Maddy, E. S., Barnet, C., Gambacorta, A., Patra, P. K., Sun, F., and Goldberg, M.: Retrieval of nitrous oxide from Atmospheric Infrared Sounder: Characterization and validation, Journal of Geophysical Research: Atmospheres, 119, 9107–9122, https://doi.org/10.1002/2013JD021406, 2014.

Zhang, Y., Sun, K., Gao, Z., Pan, Z., Shook, M. A., and Li, D.: Diurnal Climatology of Planetary Boundary Layer Height Over the Contiguous United States Derived From AMDAR and Reanalysis Data, Journal of Geophysical Research: Atmospheres, 125, e2020JD032 803, https://doi.org/https://doi.org/10.1029/2020JD032803, e2020JD032803 2020JD032803, 2020.

Zhang, Z., Eddy, W. C., Stuchiner, E. R., DeLucia, E. H., and Yang, W. H.: A conceptual model explaining spatial variation in soil nitrous oxide emissions in agricultural fields, Communications Earth & Environment, 5, 730, https://doi.org/10.1038/s43247-024-01875-w, 2024.

Zhou, Z., Liao, K., Zhu, Q., Lai, X., Yang, J., and Huang, J.: Determining the hot spots and hot moments of soil N_2O emissions and mineral N leaching in a mixed landscape under subtropical monsoon climatic conditions, Geoderma, 420, 115 896, https://doi.org/https://doi.org/10.1016/j.geoderma.2022.115896, 2022.

Zimbron, J. A., Del Grosso, S. J., and Delgado, J. A.: Measurement of nitrous oxide soil fluxes using sorbent-stabilized sampling of flux chambers, Journal of Environmental Quality, n/a, https://doi.org/10.1002/jeq2.70036, 2025.